UNIVERSITY OF CALIFORNIA, SAN DIEGO

THE ROLE OF COSTAMERIC PROTEINS IN CARDIAC FORCE TRANSMISSION AND SIGNALING

A dissertation submitted in partial satisfaction of the requirements
for the degree Doctor of Philosophy

in

Bioengineering

by

Joyce S. Chuang

Committee in charge:

Professor Jeffrey Omens, Chair
Professor Andrew McCulloch, Co-Chair
Professor Karen Christman
Professor Lawrence Frank
Professor Robert Ross

2010

The dissertation of Joyce S. Chuang is approved, and it is acceptable in quality and form for publication on microfilm and electronically:

_____

_____

_____

_____
Co-Chair

_____
Chair

University of California, San Diego

2010

TABLE OF CONTENTS

LIST OF FIGURES

LIST OF TABLES

ACKNOWLEDGEMENTS

During my five years as a graduate student, I have worked on a wide variety of projects ranging from MRI of the mouse heart to cell stretching. This dissertation is a cumulative representation of my work, which could not have been completed without the help of the people who advised and trained me.

I would first and foremost like to thank my advisor, Jeff Omens, for all his guidance, advice, and support throughout my entire five years at UCSD. Andrew McCulloch, my co-chair, also gave me invaluable input on everything from experimental design to manuscript edits. Larry Frank was instrumental in the analysis of the cardiac MRI data. The success of my *in vitro* cell study was largely dependent on the advice and resources provided to me by Robert Ross. I would like to also thank Karen Christman for her helpful suggestions and opinions during the development of my dissertation project.

Many past and present members of the CMRG lab have also spent a lot of time training me and helping me design and troubleshoot experiments. I would like to acknowledge Peter Costandi, Anna Raskin, Darlene Hunt, Amy Hsieh, Elliot Howard, Stuart Campbell, Roy Kerckhoffs, and Fred Lionetti.

From the department of Medicine, I would like to thank the following people for their expertise and advice on cell culture, RT-PCR, and mouse breeding: Alice Zemljic-Harpf, Ana Maria Manso, Hideshi Okada, Tomoko Yajima, and Farah Sheikh. From the fMRI center, I would like to thank Miriam Scadeng, Tim Salazar and Tom Liu for assisting me with the imaging of my mice.

Lastly, I want to give a heartfelt thanks to my family and friends. I am especially grateful to my parents who have always encouraged and supported me. Also, thanks to my sister, Janet, and my fiancé, Kris, for being there for me every step of the way.

Chapter 3, in part, was submitted to the *Journal of Magnetic Resonance in Medicine*, with authors Chuang JS, Zemljic-Harpf A, Ross RS, Frank LR, McCulloch AD, and Omens JH. The dissertation author is the primary investigator and author of this material.

VITA

EDUCATION

2010	PhD	Bioengineering	University of California, San Diego
2007	MS	Bioengineering	University of California, San Diego
2004	BS	Biomedical engineering	Washington University in St. Louis

HONORS AND AWARDS

- NSF graduate student fellowship, 2005-2007
- Summa Cum Laude, 2004
- St. Jude Medical Biomedical Engineering Award, 2004
- Dean's honorary scholarship, 2000-2004

ABSTRACTS

Ambrosi CM, **Chuang JS**, Yin FC. Comparison of endothelial cell gene expression to cyclic stretching versus compression, *BMES*, Nashville, TN, October 2003.

Shiekh F, Wright A, **Chuang JS**, Li C, Ouyang K, Dalton N, Gu Y, McCulloch AD, Omens JH, Peterson KL, Chen J. A Mouse Model of ARVD/C, *Keystone Symposia: Molecular Pathways in Cardiac Development and Disease*, January 2007.

Chuang JS, McCulloch AD, Omens JH, Frank L. Generation of an accurate 3D computational model of the mouse heart from MR images, *ISMRM*, Berlin, Germany, May 2007.

Chuang JS, Sheikh F, McCulloch AD, Omens JH, Frank L. Rapid, noninvasive phenotyping of the mouse right ventricle using MRI, *FASEB*, San Diego, CA, April 2008.

Chuang JS, Zemljic-Harpf A, Ross RS, McCulloch AD, Omens JH. Vinculin contributes to the passive stiffness of myocardium, *Biophysics*, Boston, MA, February 2009.

ABSTRACT OF THE DISSERTATION

THE ROLE OF COSTAMERIC PROTEINS IN CARDIAC FORCE TRANSMISSION AND SIGNALING

by

Joyce S. Chuang

Doctor of Philosophy in Bioengineering
University of California, San Diego, 2010

Professor Jeffrey H. Omens, Chair
Professor Andrew D. McCulloch, Co-Chair

Costameres are adhesion complexes that link cardiomyocytes to the extracellular matrix (ECM). In the costamere, β1D integrin links the plasma membrane to the ECM, and vinculin creates a bridge to the actin cytoskeleton. In the heart, vinculin and β1D integrin may be important for force transmission and mechanotransduction. The overall goal was to study how disruption of the costamere led to changes in ventricular mechanics, myocardial passive stiffness, and cellular hypertrophic signaling. Decoupling of ECM-cell interactions may alter ventricular regional mechanics

particularly in the sheet plane and cross-fiber direction. A technique was developed to calculate 3D ventricular strain distributions in mice using tagged MRI. End-systolic strains in vinculin deficient hearts showed that sheet extension and interlaminar shear were reduced. Structural abnormalities from costamere disruption may also affect force transmission through the costamere, which may manifest as altered material properties of the myocardium. Stretching of vinculin deficient papillary muscles revealed that a defect in the costamere resulted in more compliant tissue. In addition to its role in direct force transmission, the costamere is critical for mechanotransduction. Disruption of β1D integrin function resulted in decreased transverse stretch-induced hypertrophic signaling. In conclusion, abnormal costameres can alter LV mechanics, passive stiffness, and hypertrophic signaling. These changes can contribute to the development of dilated cardiomyopathy and the eventual onset of heart failure.

1 Introduction

1.1 Dilated cardiomyopathy

In America, approximately 5.7 million people live with heart failure, and 670,000 new cases are diagnosed each year. For 2009, the estimated direct and indirect cost of heart failure in the United States was $37.2 billion [3]. Dilated cardiomyopathy (DCM) is one of the leading causes of heart failure and cardiac transplantations in western countries [4]. Patients with DCM have enlarged hearts that are unable to pump blood effectively, which may eventually lead to arrhythmias, thromboembolic events, and heart failure [5]. DCM affects men and women as well as adults and children. DCM accounts for 55-60% of all childhood cardiomyopathies [3]. In 25-35% of these patients, DCM is genetically inherited [5]. DCM can also occur as a result of myocarditis, valvular heart disease, hypertension, and congenital heart disease. When the underlying pathology is unidentifiable, the patient is diagnosed with idiopathic dilated cardiomyopathy. Only about half of DCM patients survive five years past their

diagnosis. DCM is a major cause of cardiovascular morbidity; however, the mechanisms underlying the development of the disease remain relatively unknown.

1.2 Cytoskeletal proteins and DCM

Cytoskeletal proteins may play an import role in the development of DCM. Mutations or deletion of certain cytoskeletal proteins have been found to cause DCM in humans and animal models. In the Z-disc, defects in muscle LIM protein [6] and cypher/ZASP [7] were found to cause a DCM phenotype. Deletion or mutation of intercalated disc proteins such as α-actinin-associated LIM protein [8], plakoglobin [9], and desmoplakin [10] leads to right ventricular dilation. Mutations in lamin A/C, a nuclear membrane protein, can cause DCM and conduction-system disease [11,12]. Mutations in intermediate-filament proteins, such as desmin, are also responsible for idiopathic DCM [13]. The dystrophin-glycoprotein complex (DGC) acts as a transmembrane linker between laminin and actin. Dystrophin, a protein in DGC, has been identified as the gene responsible for X-linked dilated cardiomyopathy and is also responsible for Duchenne and Becker muscular dystrophy [14]. Mutations in δ-sarcoglycan, another DCG protein, have been linked to cases of familial dilated cardiomyopathy [15,16]. The costamere is another complex that helps adhere the cell to the extracelluar matrix. Mutations in metavinculin, a protein found in the costamere and intercalated disc, also result in LV dilation and systolic dysfunction [17]. Defective proteins in the sarcomere are generally thought to contribute to hypertrophic cardiomyopathy, a disease characterized by left ventricular hypertrophy and myofibrillar disarray [18]. However, several sarcomeric proteins have been found to be

associated with DCM: actin[19], cardiac troponin T, β-myosin heavy chain [20], and α-tropomyosin [21].

Data from human patients and genetically engineered mouse models have shown that cytoskeletal proteins play a central role in the development of DCM. In normal cardiac function, contractile force generated by the sarcomere needs to be transmitted to the plasma membrane and extracellular matrix. Many of the proteins mentioned above are thought to help link the contractile apparatus to the sarcolemma and propagate force to the extracellular matrix or to other cells. Defects in these proteins may lead to abnormal force transmission, ventricular mechanics, and eventually dilation.

1.3 Ultrastructure of cardiomyocytes

1.3.1 Sarcomere

The sarcomere is the basic contractile unit of the cardiomyocyte (Figure 1.1). Sarcomeres are joined end to end and aligned across the cell, creating the characteristic striation pattern of the cardiomyocyte. The lateral edges of the sarcomere are defined by the z-lines [1]. The z-lines are precisely aligned in order to coordinate contraction between different sarcomeres. Sarcomeres are composed of thin filaments made of actin and thick filaments made of myosin. Contraction is generated by the binding of myosin and actin molecules [22]. Antiparallel actin filaments overlap at the Z-line and are crosslinked by the actin-binding protein α-actinin. There are also noncontractile intrasarcomeric proteins such as titin. Titin acts like a molecular spring whose elasticity is largely responsible for the passive stiffness of the myocardium [23]. The N-terminal

ends of titin molecules from adjacent sarcomeres overlap at the Z-line, and the C-terminal ends extend to the M-line [24].

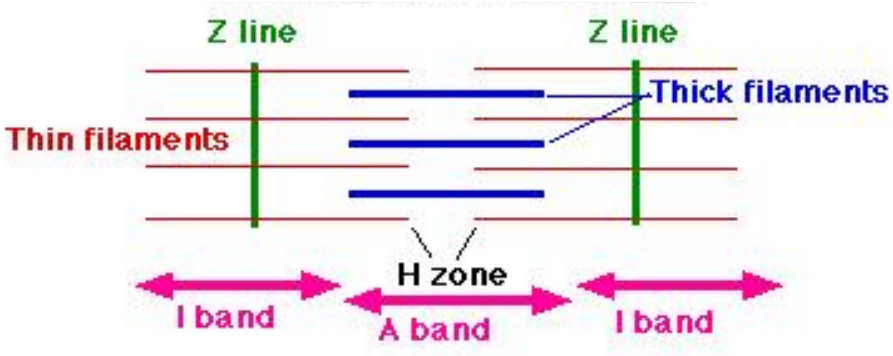

Figure 1.1: Sarcomere structure

1.3.2 Intercalated discs

In order to effectively transmit forces, the sarcomeres must be tethered to the plasma membrane. Cardiomyocytes are connected to each other at their terminal ends at cell-cell junctions called intercalated discs. The intercalated disc contains structures that help link the sarcomeric apparatus to the cell membrane. Desmosomes link the desmin intermediate filaments to the termini and fascia adherens connect the actin cytoskeleton to the membrane. Important proteins found in these structures include desmoplakin, plakophilin, plakoglobin, β and α catenin, N-cadherin, and vinculin [25]. In the intercalated discs, there are also gap junction channels made of connexin that allow for electrical coupling between cells.

1.3.3 Costamere

In the myocardium, cardiomyocytes are surrounded by extracellular matrix (ECM). The costamere is a structure that connects cardiomyocytes to the surrounding ECM. As shown in Figure 1.2, costameres are rib-like bands that surround the cardiomyocyte perpendicular to its long axis and along the Z lines [2]. The costamere consists of a protein network that creates a physical attachment between the outer Z discs and ECM. Some of the proteins found in this network include integrins, vinculin, and talin. In the costamere, integrins play an important role since they bind ECM components. Integrins are integral membrane proteins composed of α and β subunits. The β1D isoform is expressed exclusively in striated muscle and is the major β1 isoform expressed in the adult cardiomyocyte [26]. Talin binds to the cytoplasmic tails of β1D integrin, and vinculin can interact with talin and actin [27]. Thus, a molecular bridge is created between the actin cytoskeleton and ECM. It has been shown that active forces can be transmitted laterally across the cell to the ECM through the costamere [28]. Costameres are also sites where longitudinal displacement of the ECM is transmitted to the sarcomeres of the cell. A 10% static, linear stretch of aligned neonatal rat ventricular myocytes results in an immediate increase in sarcomere length by about 10% [29].

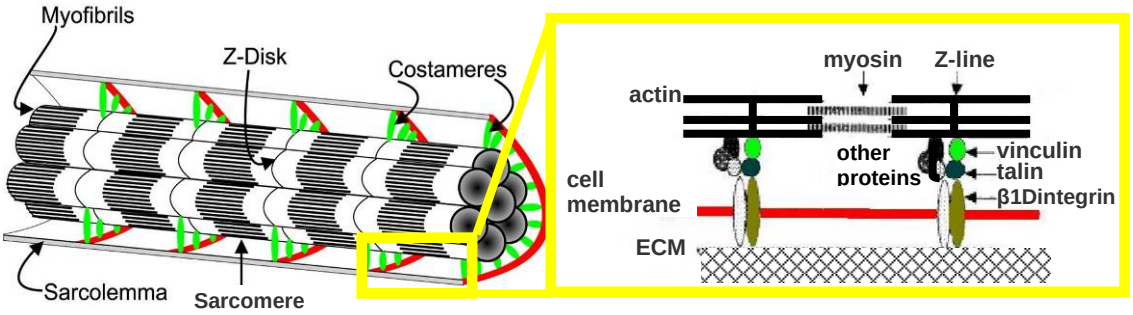

Figure 1.2: Costamere structure [2]

1.4 Myofibril and Laminar Structure

Cardiomyocytes in the *in vivo* heart are organized into higher order laminar sheets, which are critical for normal ventricular mechanics. Myofibril orientation varies from about –60º at the epicardium to +60º at the endocardium. The transmural distribution of the fiber angle is thought to make the distribution of active fiber stress and strain more homogeneous across the left ventricle [30]. The fibers are organized into branching laminar "sheets", approximately 4 cells in thickness [31]. Fibers within a sheet are tightly coupled, and adjacent sheets are loosely coupled by collagen. These features make the myocardium an orthotropic tissue [32]. The sheet structure is thought to provide the basis for the rearrangement of cardiomyocytes during systolic ventricular thickening predominantly through interlaminar shear and sheet extension [33,34]. The fiber and laminar structures are also important during diastole. During early relaxation, there is significant stretch along epicardial myofibers and sheet shortening and shear in the endocardial layers. The deformations of the fiber and sheet structures may help torsional recoil and early diastolic filling [35,36].

1.5 Mechanotransduction

The costamere plays an important role in physically linking the actin cytoskeleton to the ECM through protein-protein interactions. In addition to this structural role, costameres also have an important signaling role in the myocardium. In a healthy heart, pressure overload will induce a hypertrophic response where the cells remodel and enlarge to compensate for the elevated ventricular stresses. Integrins in the costameres can act as mechanosensors and activate intracellular signaling cascades in response to an increase in mechanical overload. These molecular signals lead to changes in gene expression such as the induction of atrial natriuretic factor (ANF) and b-type natriuretic peptide (BNP) [37].

In the costamere, integrins are transmembrane proteins that are positioned to transduce physical forces at the plasma membrane into cytoplasmic chemical signals. Integrin mediated hypertrophic signaling has been associated with several early signaling molecules. Focal adhesion kinase (FAK) is activated in cardiomyocytes exposed to cyclic stretch and in pressure overloaded myocardium [38]. Inhibition of FAK phosphorylation also leads to lower ANF expression. FAK can bind to β1 integrin tails [39]. Upon integrin binding, autophosphorylation of Tyr-397 occurs, thus, creating a strong binding site for c-Src [40]. The Fak/Src complex can lead to activation of ERK1/2 [41]. FAK has also been shown to activate the p38MAPK during stretch induced hypertrophy [42] as well as the JNK pathway [43]. The Grb2/SOS complex can also bind to phosphorylated Tyr-397 and lead to activation of Akt hypertrophic pathway [41].

Integrin linked kinase (ILK) is another signaling molecule located in the costamere. It is upregulated during hypertrophy [44]. In a constitutively active ILK model, p38 MAPK and ERK1/2 activation leads to hypertrophy [44]. ILK is stimulated in a phosphatidylinositol 3-kinase (PI-3 Kinase) dependent manner [45]. PI-3 Kinase is also known to be activated by cyclic stretch in cardiomyocytes [46]. Activated ILK can also phosphorylate PKB/Akt, which leads to the growth response in myocytes. ILK knockout mice show a dilated cardiomyopathy phenotype and Akt phosphorylation is decreased too [47]. ILK also plays a role as an adaptor protein which links the actin cytoskeleton to the ECM (Fig. 4). ILK binds to cytoplasmic tail of β1D integrin and the actin binding protein parvin, thus creating a molecular scaffold from the integrin to cytoskeleton [48].

1.6 Integrin

β1 integrin has four isoforms, but the β1D isoform is expressed only in striated muscle and is the major isoform expressed in the postnatal myocyte. β1A integrin is expressed ubiquitously and is present in the embryonic heart [49]. Integrins are important in the maintenance of healthy cardiac structure and function. Homozygous β1 integrin null embryos are able to develop to the blastocyst stage, but die shortly after embryo implantation in the uterine wall [50]. In a cardiac specific β1 integrin KO mouse model, β1D isoform was reduced to 18% of control wildtype levels. Although the mice survived to adulthood, a variety of cardiac abnormalities arose. These mice showed myocardial fibrosis, depressed LV function, and intolerance to hemodynamic loading. Evan's blue dye stain showed compromised cardiomyocyte membrane

integrity. Positron emission tromography also showed that β1KO hearts had abnormal myocardial glucose metabolism. By 6 months of age, β1KO mice had developed dilated cardiomyopathy and died spontaneously [51].

Integrin expression increases in the presence of hemodynamic loading [52]. When integrin function was disrupted, basal levels of phosphorylated FAK were decreased, and aortic banding failed to induce changes in the levels of phosphorylated FAK or ERK [53].

1.7 Vinculin

Vinculin (Vcl) is an actin-binding protein found in intercalated discs, focal adhesions, and costameres. In addition to actin, Vcl can also bind to talin [54]. The binding of talin to cytoplasmic integrin tails can activate integrins and alter their affinity for ECM ligands [55]. Since Vcl binds to both actin and talin, it physically couples the cytoskeleton to the ECM and may play a role in mechanotransduction.

In cell culture, Vcl has been shown to regulate cell spreading, motility and adhesion. In embryonic fibroblasts used in FRET-based studies, Vcl is activated when localized to focal adhesions. In its activated conformation, Vcl can bind to talin and actin [56]. Recruitment of Vcl to focal adhesions increases the cell's adhesion strength [57]. Atomic force microscopy of Vcl deficient F9 embryonic carcinoma cells showed that cell stiffness decreases in the absence of Vcl [58]. Thus, Vcl helps stabilize focal adhesions and strengthen cell-matrix interactions. Vcl has also been shown to regulate activation of FAK. Interaction between the adaptor protein paxillin and FAK is important for the induction of certain signaling pathways. Vcl can inhibit binding of

paxillin to FAK. Vcl null cells exhibit increased paxillin and FAK binding, FAK phosphorylation, and ERK activation [59].

In vivo studies have shown that Vcl is important for maintaining cardiac structure and function. In homozygous global VclKO mice, death occurs at embryonic day 10.5 with neural defects, aberrant forelimb development, and reduced heart size [60]. Heterozygous VclKOs survive to adulthood and reproduce; however, they are predisposed to heart failure when challenged by hemodynamic loading and show misalignment of α-actinin containing Z-lines [61]. Cardiac specific VclKOs have enlarged left ventricles, increased ventricular mass, fibrosis, and reduced systolic/diastolic function. Expression of cadherin and β1D integrin is also reduced. At 9 weeks of age, hypertrophy is present with increased levels of ANF and BNP [62].

1.8 Conclusions

DCM is a disease that usually progresses to heart failure and death. By better understanding the mechanisms in which DCM arises, we can help improve cardiac function and survival in affected patients. Many genetic studies have shown that defects in cytoskeletal proteins are associated with DCM. These proteins are involved in structural connections from the internal sarcomere lattice to the cell membrane, and play important roles in force transmission between cells and to the extracellular matrix. Disruption of these linkages may alter the force transmission, which results in ventricular dysfunction and dilation. In addition to the physical propagation of force, these proteins may contribute to the propagation of molecular signals in the cardiomyocyte. For example, impairment of mechanotransduction pathways may lead

to heart failure by weakening the compensatory hypertrophic response of the cardiomyocyte.

The studies presented in this dissertation investigate the role of costameric proteins in force transmission and mechanotransduction. In the costamere, β1D integrin connects the plasma membrane to the ECM, and Vcl creates a bridge to the cytoskeleton. These proteins may be important for force transmission and transduction of force into biochemical signals. To study the role of Vcl and β1D integrin in the heart, we utilized knockout mouse models as well as isolated cell preparations. We hypothesized that deletion or disruption of these proteins would alter left ventricular mechanics, passive material properties, and/or hypertrophic signaling. Elucidating the mechanical and biochemical mechanisms in which cytoskeletal defects lead to DCM may eventually help us develop therapeutic treatments to stop or reverse progression of this disease.

1.9 Scope of the Dissertation

The objective of this dissertation was to investigate the role of costameric proteins in cardiac force transmission and mechanotransduction. We studied the effect of Vcl deletion on ventricular mechanics and passive material properties, and the effect of β1D integrin disruption on anisotropic hypertrophic signaling.

Chapter 2 describes the development and validation of a method that quickly and accurately reconstructs the ventricles of the live mouse heart from high spatial resolution and temporally resolved high field MR images.

Chapter 3 describes a method that combines MRI tagging, automated material point tracking, and anatomically accurate finite element models to calculate non-homogeneous 3D finite strain distributions in the mouse LV throughout the cardiac cycle. The method was used to calculate 3D cardiac strains in the VclKO mouse model of dilated cardiomyopathy at 8 weeks of age.

Chapter 4 describes how fiber and sheet strains were altered in 6 week old VclKO mice prior to the onset of cardiac dysfunction. Fiber and sheet angles were measured with histology and 3D cardiac strains from MR tagging were transformed into fiber/sheet coordinates.

Chapter 5 describes the effect of Vcl deletion on the passive material properties of myocardial tissue. Murine RV papillary muscles of Vcl deficient hearts were stretched and stress-strain curves were measured to calculate passive stiffness.

Chapter 6 describes a study where β1D integrin function was disrupted by overexpression of the cytoplasmic domain of β1D integrin. We hypothesized that β1D integrin function disruption would abolish directional sensitivity to stretch such that transverse stretch would induce levels of ANF similar to those produced by longitudinal stretch.

Chapter 7 summarizes these studies and their contributions to our understanding of costameric proteins and their role in the development of dilated cardiomyopathy.

2 Three-dimensional anatomical modeling of the mouse heart

2.1 Introduction

Historically, large animal models have been used for cardiovascular disease research; however, the mouse model has become a popular tool within the last decade [63]. Surgical methods such as aortic banding [64] and myocardial infarction [65] can be used to induce pathological changes in the mouse heart, and genetic modification of the mouse also allows us to study the molecular origin of different diseases [66]. However, studying the mouse heart *in vivo* can be challenging due to the fast heart rate and small heart size.

Several techniques are commonly used to characterize the *in vivo* mouse cardiac phenotype: echocardiography [67], micro computed tomography (CT)[68], and MRI. Echocardiography is fast and relatively inexpensive; however, it suffers from lower

signal-to-noise ratio (SNR) and geometric assumptions are necessary for cavity volume estimations with M-mode echocardiography. MicroCT offers high tissue contrast but exposes animals to ionizing radiation which may be detrimental for longitudinal studies. MRI is considered the gold standard for noninvasive imaging of the mouse heart due to its high spatial and temporal resolution, but it is relatively expensive. MRI has been used to quantify global geometry and function in the mouse heart. The Simpson's rule [69-71] is widely used to calculate LV and RV cavity and wall volumes. It is based on the idea that the volume of an object can be determined by cutting the object into thin slices, measuring the volume of each slice, and summing the volumes of all slices. The Simpson's rule is a numerical integration of the myocardial or cavity areas in each 2D slice; therefore, 3D geometric information is lost with this method of analysis.

We have created and validated a method that quickly and accurately reconstructs the ventricles of the live mouse heart from high spatial resolution and temporally resolved high field MR images. Our technique optimizes image acquisition for complete spatial coverage of the heart, thus collecting sufficient data to model both ventricles. Important geometric and functional values such as cavity volumes, ejection fraction, wall mass, and wall thickness can be extracted from these 3D models. The resulting 3D geometry can also be directly incorporated into finite element (FE) analysis.

Our technique was validated and also tested in two mouse models of cardiovascular disease with known changes in geometry and function. Aortic banding was performed to induce LV pressure overload and hypertrophy in the wildtype (WT)

mouse. Also, a cardiac specific desmoplakin knockout (DP KO) mouse was used as a model of arrhythmogenic right ventricular dysplasia/cardiomyopathy (ARVD/C) [72], a disease characterized by RV dilation and dysfunction.

2.2 Methods

2.2.1 Mice

Black Swiss mice were used for the aortic banding study (National Cancer Institute Jackson Laboratories, Sacramento, CA). The mice were male and between 2-3 months of age. Six-week old DP KO mice and their wildtype (WT) littermates were provided by the Ju Chen lab at the University of California, San Diego. All protocols were performed according to the National Institutes of Health *Guide for the Care and Use of Laboratory Animals* and approved by the UCSD Animal Subjects Committee.

2.2.2 Surgery

Ascending aortic banding was used to produce left ventricular pressure overload in the mice. Black swiss mice were anesthetized with intraperitoneal ketamine-xylazine, intubated, and ventilated with room air. Aortic constriction was performed by placing a ligature (6-0 Ethalon) securely around the ascending aorta and a blunted 26-gauge needle and then removing the needle. After banding, the thoracic cavity was closed. The mice were extubated and placed in recovery cages vented with 100% oxygen until they were fully recovered from anesthesia. For the sham operations, the same steps were followed except no suture was tied around the aorta.

2.2.3 Cardiac cine MRI

The mice were imaged under free breathing inhaled isoflurane anesthesia. The mice were initially sedated with 5 vol-% isoflurane in 100% O_2. Then the mice were transferred into a restraint unit centered within a custom built 3 cm RF coil. In the coil, the mouse remained sedated in a supine position with 1 vol-% isoflurane being delivered through a nose cone at 1.5 L/min. MR compatible ECG leads were inserted subcutaneously into the front paws of the mouse. ECG monitoring was performed with a control gating module (SA Instruments, Stony Brook, NY). The heart rate was maintained at 450-500 BPM. During the scan, the bore temperature was regulated using heated airflow to maintain the mice at 36-38°C. The MRI protocol was performed on a 7T Varian horizontal-bore magnet capable of a 740 mT/m gradient strength and 250 mT/m/ms slew rate.

For cine MRI of the mouse heart, an ECG triggered fast gradient echo pulse sequence was used. Scanning parameters were optimized for signal to noise: echo time (TE) = 1.2 ms, repetition time (TR) = 5 ms, flip angle = 20°, and averages = 4. A field of view of 2.5 cm and data matrix of 128 X 128 were prescribed for an in-plane resolution of 195 um, and the slice thickness was 1 mm. In one cine acquisition ≈20 phases within the cardiac cycle were collected depending on the heart rate.

In the imaging protocol, the long axis of the LV was first identified. Then a short axis slice through the mid section of the LV was acquired (Figure 2.1A). From the short axis image, five longitudinal slices were prescribed (Figure 2.1B). The first longitudinal slice bisected the septal wall and each successive slice was separated

radially by 36°. The five longitudinal slices were centered and intersected along the long-axis of the LV. For RV reconstruction, three additional short-axis slices covering the RV were acquired (Figure 2.1C).

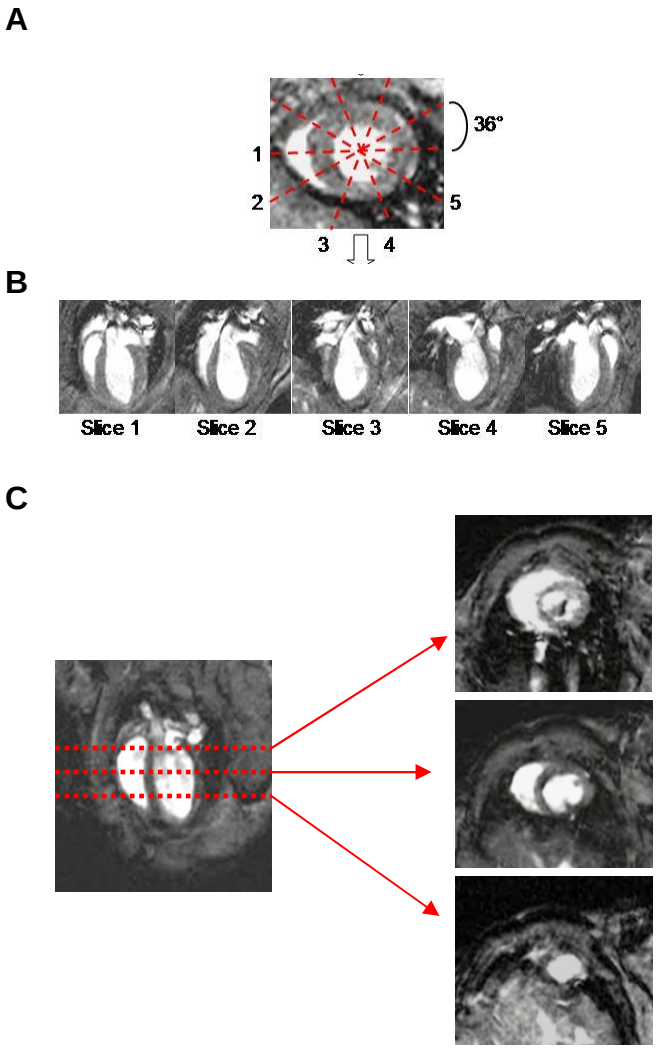

Figure 2.1: Cine imaging protocol includes 5 long-axis slices for LV reconstruction (A and B) and 3 additional short-axis slices for RV reconstruction (C).

2.2.4 Image analysis

For each cine acquisition, the end-diastolic frame was chosen as the image with the largest LV cavity and the end-systolic frame was the image with the smallest LV cavity. With cine gradient echo imaging, the blood appears brighter than the myocardium. Edge detection filters in MATLAB were used to help define the epicardium, RV endocardium, and LV endocardium (Figure 2.2).

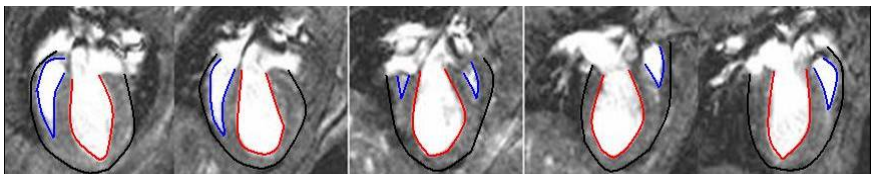

Figure 2.2: Epicardial (black) and endocardial boundaries of LV (red) and RV (blue)

2.2.5 Finite element model

The points of the edges were imported into Continuity 6, a finite element package (Figure 2.3A). The long-axis of the LV was chosen such that the sum of squares of the distances between the data points and axis was minimized. The 3D coordinates were converted to prolate spheroid coordinates in order to reduce the surface fit to one dimension. 2D prolate spheroidal meshes (Figure 2.3B) were fit to the endocardial and epicardial data points using a least squares minimization of the λ coordinate using bicubic and cubic-linear basis functions. The 2D meshes were linearly coupled to form a 3D mesh. The resulting mesh was converted to 3D rectangular Cartesian coordinates with tricubic basis functions. The mesh of the LV alone contained 40 elements, and the biventricular mesh contained 64 elements: 6 RV free

wall elements, 6 septum wall elements, 26 LV endocardium elements, and 26 epicardial elements (Figure 2.3C). Cavity and element volume were measured directly from the 3D mesh. To calculate wall mass, the wall volume was multiplied by a myocardial density of 1.05 g/ml.

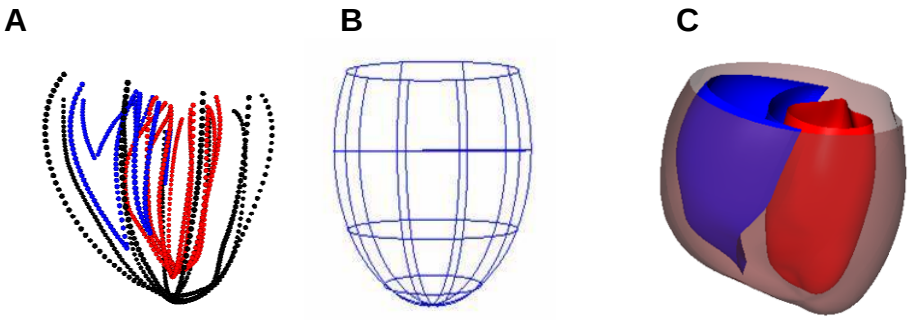

Figure 2.3: Dataset (A) and prolate spheroidal meshes (B and C). Red indicates the LV and blue indicates the RV

2.2.6 Statistics

All measurements are presented as mean ± SD. Linear regression analysis was used compare necropsy and mass measurements. Student's *t*-test was used to compare geometric and functional parameters. Aortic banding data was analyzed with the paired Student's *t*-test. P values < 0.05 were considered significant.

2.3 Results

2.3.1 Validation

In order to validate our 3D reconstruction technique, mass measurements from the models were compared to direct wet-weight mass (blood removed from chambers) from necropsy measurements of the same mouse hearts. For LV models, linear regression analysis showed a strong correlation between the model-derived mass and

necropsy-derived mass with a correlation coefficient of 0.98 (Figure 2.4A). Linear regression analysis of biventricular models also showed good agreement between wet-weight mass and model-derived mass with an R value of 0.98 (Figure 2.4B).

A

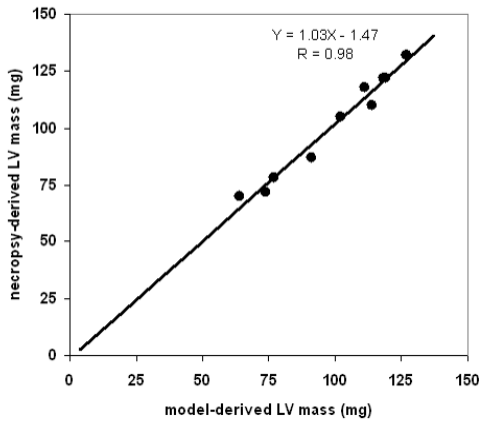

B

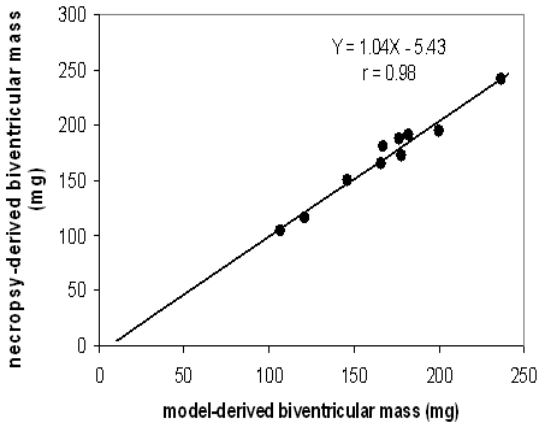

Figure 2.4: Mass validation of LV models (A) and biventricular models (B)

In addition to mass validation, stroke volumes (SV) of both ventricles can be measured for validation of biventricular models. Under physiological conditions where valves are competent, the SVs of the ventricles are expected to be equal [71]. Thus, the left ventricular SV provides an internal standard for the right ventricular SV. Linear regression analysis showed a strong correlation with R = 0.93 (Figure 2.5).

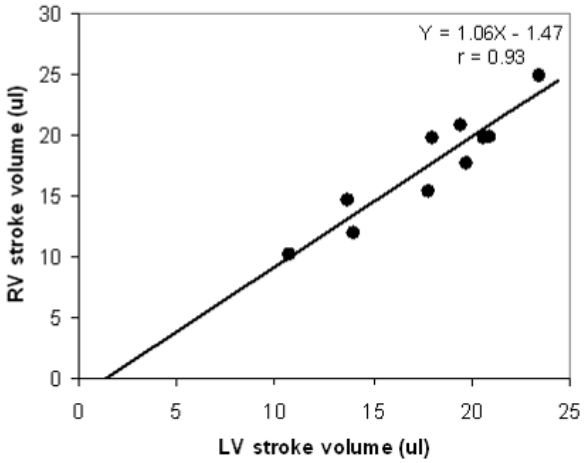

Figure 2.5: Stroke volume validation of biventricular models

2.3.2 Ascending aortic banding model

Ascending aortic banding was performed to induce the hypertrophic response in the LV. The mice were imaged prior to the surgery and 4 weeks later (n = 4). Figure 2.6 shows end-diastolic MR images of a sham operated heart and a banded heart 4 weeks after the surgery. Their respective 3D models are also shown. As expected, the ventricular wall of the banded heart was thicker than the sham operated heart.

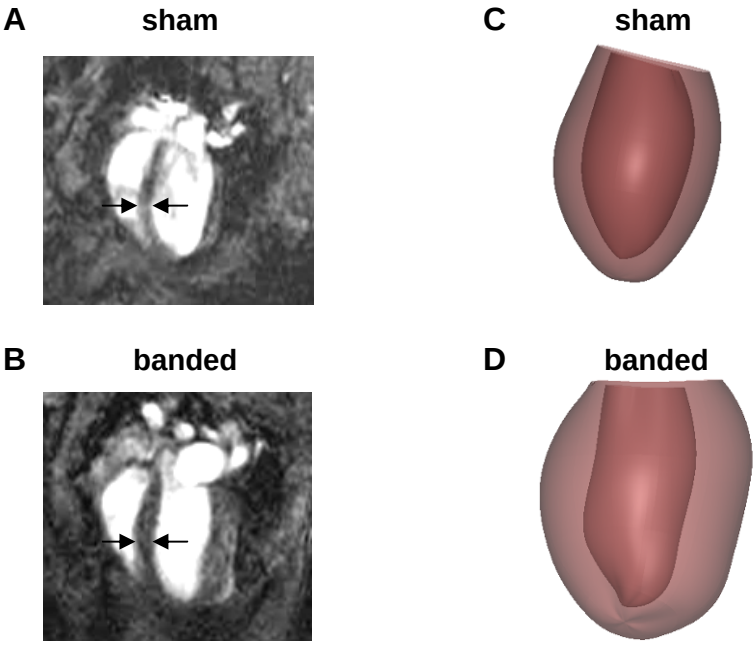

Figure 2.6: MR images and 3D models of normal and banded hearts.

LV mass was normalized by body weight (LVMI). One month after aortic constriction, LVMI had increased significantly above pre-banding levels (Figure 2.7). In sham-operated hearts, LVMI remained unchanged.

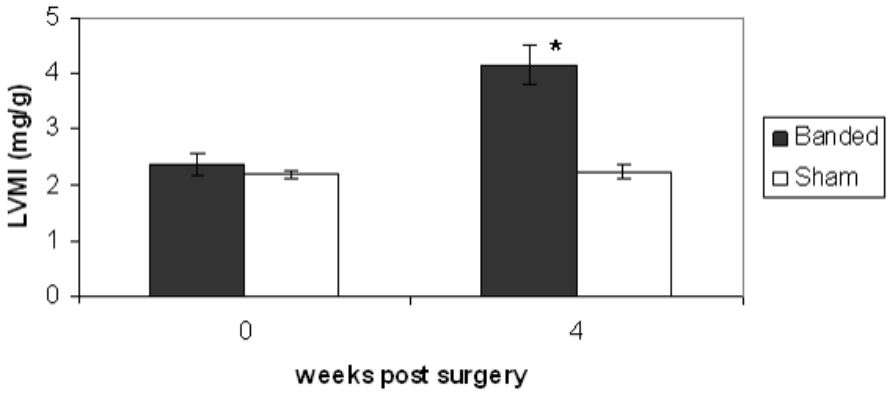

Figure 2.7: LVMI of banded and sham-operated hearts. One month after banding, LVMI was significantly higher in banded hearts ($P < 0.05$*).

2.3.3 DP KO model

DP KO mice were imaged at 6 weeks of age when dilation and cardiac dysfunction were present. Figure 2.8 shows end-diastolic MR images of a representative WT and DP KO heart and their corresponding 3D models. Both ventricles in the DP KO heart appear larger than in the WT heart.

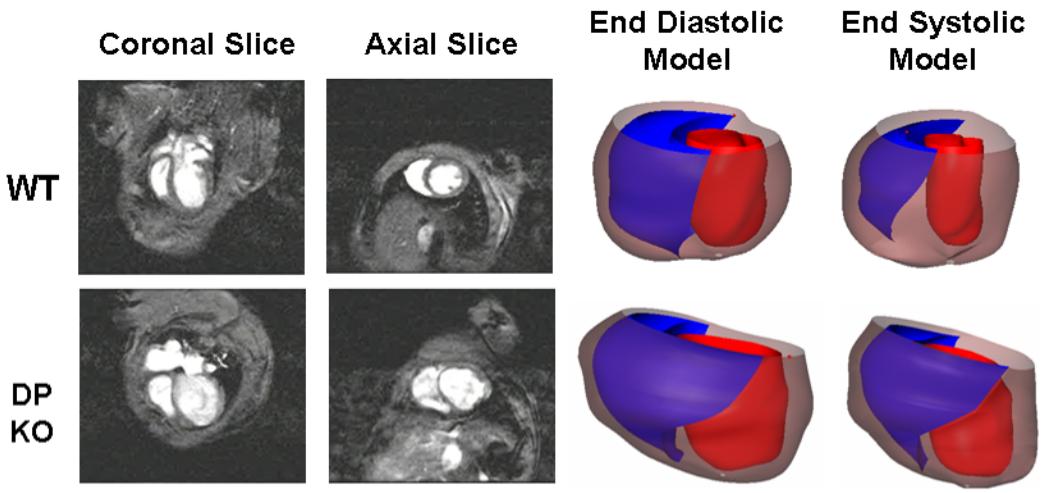

Figure 2.8: MRI and 3D models of DPKO and WT hearts.

In the WT hearts, the chamber volumes and ejection fraction were within the expected levels. In the DP KO mice, both ventricles were dilated and almost double the volume of the WT ventricles (Table 2.1). In both ventricles, the ejection fractions of the DP KOs were significantly lower than the WT values.

Table 2.1: Global functional data of DP KOs shows chamber dilation and decreased ejection fraction compared to WTs.

	LV EDV (µl)	LV ESV (µl)	LV EF (%)	RV EDV (µl)	RV ESV (µl)	RV EF (%)
WT	44 ± 5	21 ± 3	53 ± 3	44 ± 6	25 ± 4	43 ± 4
DP KO	85 ± 7*	67 ± 5*	22 ± 1*	81 ± 13*	67 ± 13*	18 ± 3*

*P < 0.05 WT vs. DPKO

2.4 Discussion

We developed a technique for creating 3D FE models of the *in vivo* mouse heart from high-resolution, temporally resolved high field MR data. The image acquisition protocol collects detailed spatial data to accurately reconstruct the ventricular geometry at different time points during the cardiac cycle. The results were validated with direct necropsy mass measurements and stroke volume comparisons. Our technique was also able to capture global geometric and functional changes resulting from a surgical intervention or genetic defect.

Using our technique, we were able to detect global changes in the mouse LV after aortic banding. As expected, the sham groups showed fairly constant LVMI throughout the entire study. In WT banded mice, the hypertrophic response was activated by the LV pressure overload. As expected, the LVMI increased after banding and was significantly higher than the sham group. A month after banding, the LVMI was almost double the sham value, which is consistent with published literature [73].

We were also able to characterize the more complex, asymmetric geometry of the RV. DP KO mice were imaged as a model of ARVD/C, a genetic disease characterized by RV dysfunction, fibrofatty deposits, and sudden death. Several DP mutations have been identified in human patients with ARVD/C [72]. DP is a protein abundantly expressed in the desmosome. The desmosome is an intercellular junction that links adjacent cells tightly together, and DP binds the intermediate filaments and helps anchor them to the cell membrane [74]. 3D models of the DP KO hearts show that the mice suffer from a cardiomyopathy that affects both ventricles. The RV and LV were found to be dilated and ejection fractions were decreased from WT levels. Human cases of ARVD/C are also characterized by enlargement of the RV and diminished ejection fraction.

The presented technique not only allows for the calculation of cavity and wall volumes of the mouse heart, but it creates a 3D model which can be used in a variety of computational experiments. FE model simulations of human or large animal hearts have already advanced the understanding of ventricular biomechanics and electrical activation in diseased states [75]. It is important for these models to have realistic cardiac geometries since diseased hearts are typically abnormal in shape and size. Our technique provides an accurate anatomical framework for mechanical and electrophysiological simulations of the mouse heart.

3 Determination of three-dimensional ventricular strain distributions in gene-targeted mice using tagged MRI

3.1 Introduction

The mouse has become an important model in cardiovascular research. Gene-targeted mice are frequently used to study the molecular basis of cardiac diseases. In doing so, mouse models of cardiomyopathies with inherent ventricular hypertrophy, dilatation, or diastolic/systolic dysfunction are created and analyzed using a range of physiological techniques [63,66,76,77]. Despite the progress in using these models to study the biological basis of cardiovascular disease, measuring regional cardiac function *in vivo* in the mouse is challenging due to the small size and fast beating rate of the mouse heart. Magnetic resonance imaging (MRI) is a technique commonly used to

quantify global geometric and functional parameters of the mouse heart *in vivo* such as wall mass, cavity volumes, stroke volume, and ejection fraction [69,78-80]. With MR tagging techniques, myocardial motion and regional strain can also be studied. Ventricular torsion [81,82] and 2-D strains [83-85] have been measured in the mouse LV using MR tagging.

Nevertheless, for a complete description of myocardial tissue deformation, the spatial distributions of the nonhomogeneous 3D strain tensor components need to be measured throughout the ventricular myocardium, including transmurally. Regional heterogeneities in function are important to characterize, particularly in diseased hearts. For electrical function, transmural regional heterogeneity of action potentials plays a role in the development of arrhythmias in the heart [86]. Spatial gradients in proteins such as phosphorylated myosin light chain are thought to facilitate torsion of the heart [87]. In dilated cardiomyopathy (DCM), the transmural gradient in radial strain is reduced, which can adversely affect global function [88]. Using tagged MRI, 3D strains have been measured in healthy and diseased large animal [89,90] and human [91-93] hearts. In the mouse heart, 3D strains from MR tagging have been calculated by adopting techniques used in larger hearts such as homogenous strain analysis [94] or finite element analysis [95]. Previous studies have mainly focused on characterizing function in normal hearts or myocardial infarction models [64]; however, MRI has yet to be shown capable of measuring regional function in genetically engineered mouse models of cardiovascular disease.

Here we describe a method that combines MRI tagging, automated material point tracking using HARP, and anatomically accurate finite element models to calculate non-homogeneous 3D finite strain distributions in the mouse LV throughout the cardiac cycle. These methods were sufficiently sensitive to detect significant regional differences in systolic wall thickening and shear strains between a genetically engineered mouse model and WT littermate controls, prior to the onset of overt heart failure. End-systolic radial strain and torsional shear were reduced in genetically engineered hearts and found to contribute to a decreased ejection fraction.

3.2 Methods

3.2.1 Mouse model

A mouse model with cardiomyocyte-specific excision of the vinculin gene (VclKO) using Cre-LoxP technology [62] was previously characterized by us and seen to develop overt DCM by 16 weeks of age. Eight week-old male VclKO mice (n = 5) and WT littermates with no Vcl excision were used for the MRI study. All protocols were performed according to the National Institutes of Health's *Guide for the Care and Use of Laboratory Animals* and approved by the UCSD Animal Subjects Committee.

3.2.2 Animal preparation and monitoring

The mice were initially sedated with 5 vol-% isoflurane in 100% O_2 and transferred to a custom built restraint unit which was centered within a quadrature volume coil with an inner diameter of 2.5 cm (Bruker, Germany). In the RF coil, the mouse remained sedated in a supine position with 1.5 vol-% isoflurane being delivered through a nose cone at 1.5 L/min. MR compatible ECG leads were inserted

subcutaneously into the front paws of the mouse. ECG and body temperature were monitored with the MR compatible SAII Model 1025 monitoring and gating system (SA Instruments, Inc., Stony Brook, NY, USA). The heart rate was maintained at 400 ± 10 BPM. The bore temperature was regulated using heated airflow to maintain the mice at 36-38°C.

3.2.3 MRI

The MRI protocol was performed on a 7T horizontal-bore magnet (Varian, Palo Alto, CA, USA) with an Avance II console (Bruker, Germany). The scanner is equipped with a gradient system capable of 100mT/m gradient strength and maximum ramp time of 210 μsec.

An ECG-triggered 2D fast gradient echo pulse sequence was used for cine imaging with the following parameters: echo time TE = 2.3 ms, repetition time TR = 6 ms, flip angle α = 15°, slice thickness 1 mm, and 4 averages. A field of view of FOV=2.0 cm and data matrix of 128·128 were prescribed for an in-plane resolution of $(156\ \text{um})^2$. Depending on the heart rate, 20-23 cardiac phases were reconstructed.

For MRI tagging, a Spatial Modulation of Magnetization (SPAMM) sequence was used to create images with a periodic pattern of stripes that move with the heart wall [96]. A tagging module (7 ms duration) was applied after the detection of the R wave to produce a tagging grid with a tag distance of 0.9 mm and tag width of 0.31 mm. All other parameters were matched to the cine image acquisition except for increasing the number of averages to 20.

In the image acquisition, the long axis of the LV was first identified. Five short axis slices perpendicular to the long axis of the LV were acquired. Then 3 longitudinal slices centered about the long axis of the LV were obtained (Figure 3.1). The first long axis slice bisected the septal wall and each successive slice was separated radially by 60°. Both cine and tagged images were acquired for all slice locations. The entire imaging protocol took approximately 1 hour for each mouse.

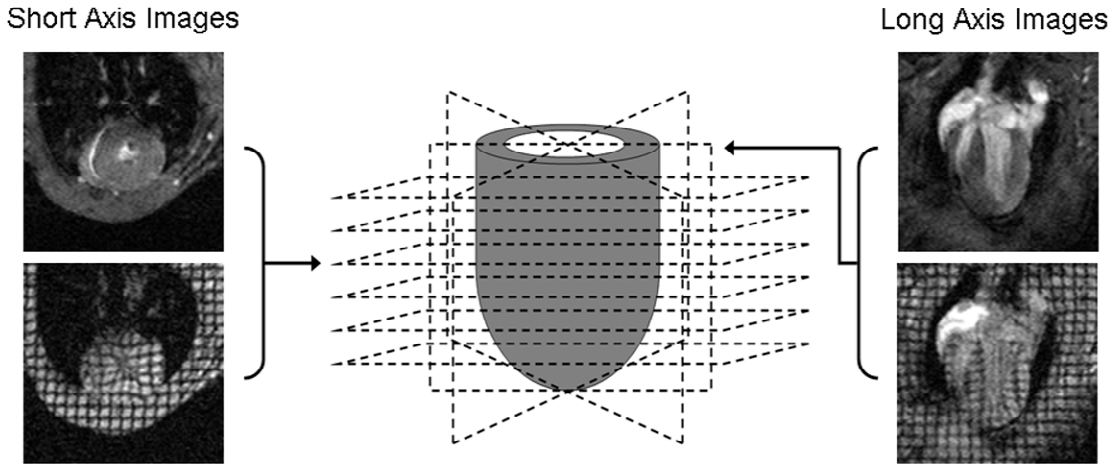

Figure 3.1: Imaging protocol includes 5 short axis slices and 3 long axis slices. Both cine and tagged images are acquired at each location.

3.2.4 Image analysis

For each slice location, the first frame of the cine acquisition was used for segmentation of the LV myocardium at end-diastole. A semiautomatic level set algorithm available in the ITK-SNAP software [97] was used to extract the LV endocardial and epicardial boundaries.

The SPAMM image sequence corresponding to the same slice location was used for 2D material point tracking. Harmonic Phase (HARP) analysis was used to

automatically track material points through the cardiac cycle [98]. First, the end diastolic frame of the SPAMM image sequence was transformed by a 2D Fast Fourier Transform (FFT) into the frequency domain. The spectral peak located at the first positive harmonic frequency in each tag direction was isolated with a bandpass filter. The inverse FFT of each filtered spectral peak results in a complex image from which a phase map is obtained (Figure 3.2).

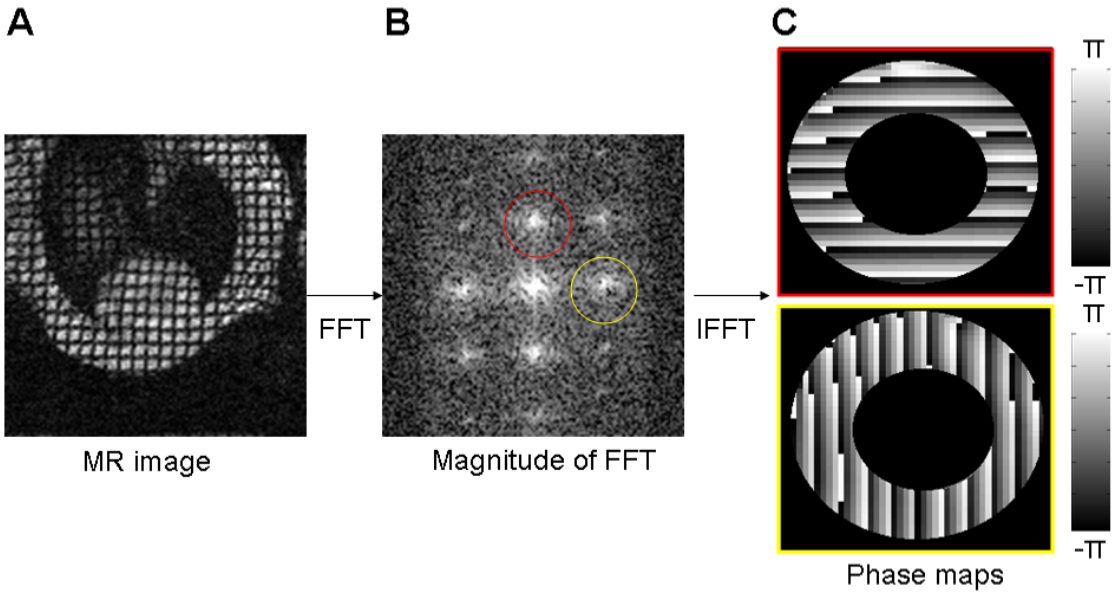

Figure 3.2: The tagged image (A) is transformed into the frequency domain (B) and spectral peaks are isolated to produce phase maps (C).

A material point contains a pair of phases (one for each tag direction) which are time invariant. However, the phase maps contain wrapping artifacts, so no unique solution can be found. When tracking a material point from one time frame to the next, it is assumed that the correct match is the one closest to the point location in the initial frame. Due to the discrete nature of the images, linear interpolation can be used to find phase positions with subpixel resolution. Using HARP analysis, the 2D displacement of

a material point can be calculated. In both short and long-axis tagged images, points located at the center of each pixel within the LV myocardium were tracked in 2D through the cardiac cycle (Figure 3.3).

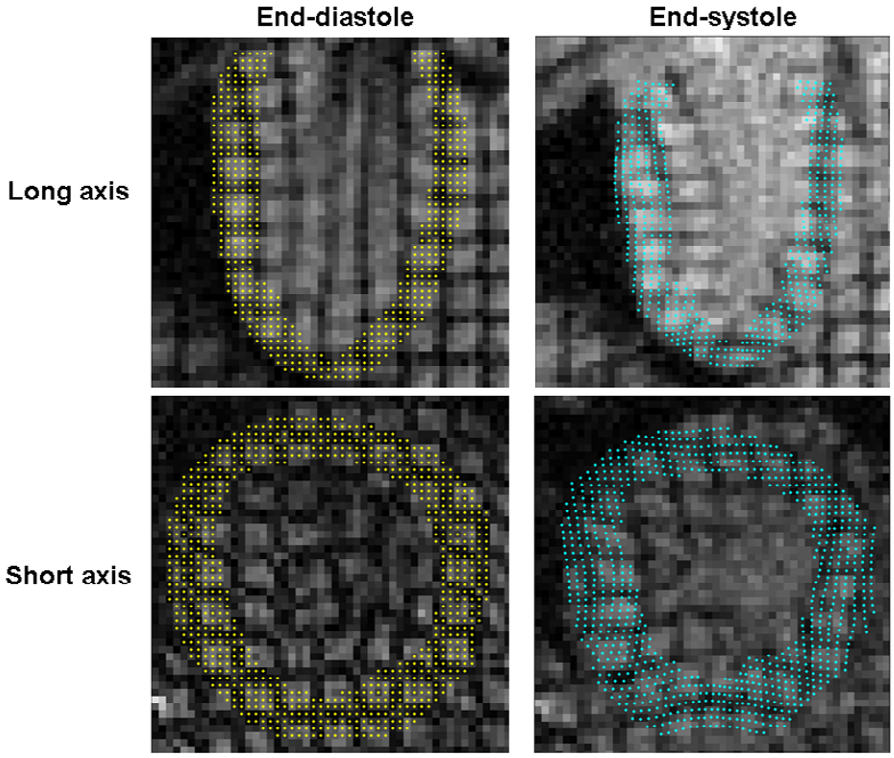

Figure 3.3: Material points are tracked from end-diastole to end-systole using HARP.

3.2.5 Geometric model

A geometric model of the LV at end-diastole was created using prolate spheroidal bi-cubic Hermite finite element surface meshes (Figure 3.4A) which were fit to LV endocardial and epicardial boundary points [99,100]. The fit was performed using a least squares minimization of the λ coordinate with bicubic Hermite interpolation. A 3D bicubic-linear mesh was created from the endocardial and

epicardial surfaces (Figure 3.4B) and then converted into 3D rectangular Cartesian coordinates that were all interpolated with tricubic basis functions. The final mesh has 16 elements (Figure 3.4C). The mesh is oriented such that the X-axis lies along the long-axis of the LV and the Y-axis bisects the septal wall. Cavity and element volumes can be measured directly from the 3D mesh. Wall mass is calculated by multiplying wall volume by the myocardial density (1.05 g/ml).

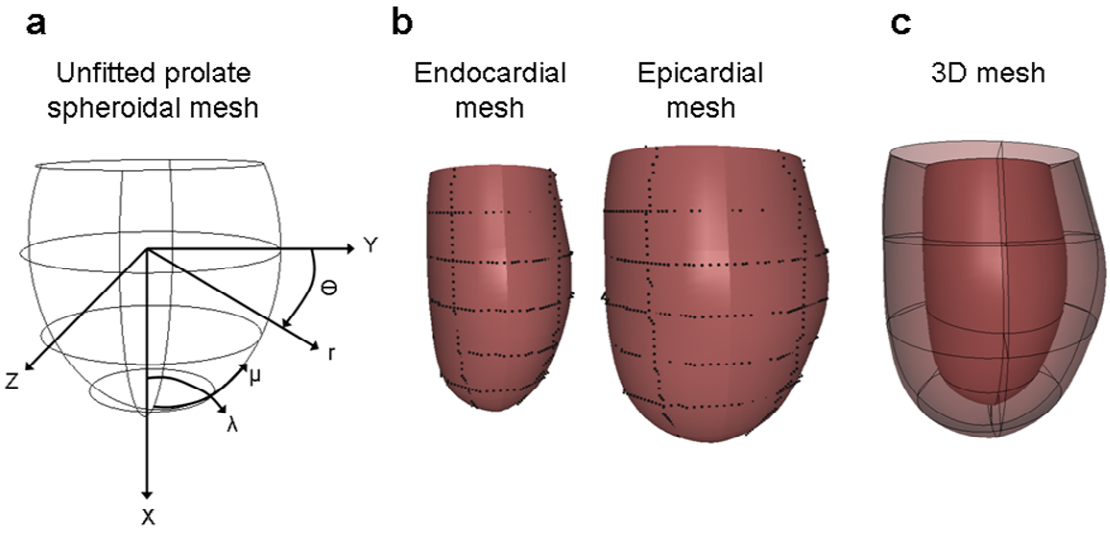

Figure 3.4: Prolate spheroidal mesh (a) is fitted to endocardial and epicardial points (b) to create a 3D mesh of the LV (c).

3.2.6 Strain analysis

A deformable model was used to calculate Lagrangian 3D strains throughout the LV. The end-diastolic geometry is used for the undeformed reference state. The model is deformed to fit material point coordinates throughout the cardiac cycle using a least squares fit of tricubic Hermite deformed nodal coordinate parameters with the following objective function [101]:

$$F(\mathbf{X}) = \sum_{d=1,D} \gamma_d \left\| \mathbf{X}(\zeta_d) - \mathbf{X}_d \right\|^2 + \int_\Omega \left\{ \alpha \left(\left\| \frac{\partial \mathbf{u}}{\partial \zeta_1} \right\|^2 + \left\| \frac{\partial \mathbf{u}}{\partial \zeta_2} \right\|^2 \right) + \beta \left(\left\| \frac{\partial^2 \mathbf{u}}{\partial \zeta_1^2} \right\|^2 + \left\| \frac{\partial^2 \mathbf{u}}{\partial \zeta_2^2} \right\|^2 \right) + \alpha^2 \left\| \frac{\partial^2 \mathbf{u}}{\partial \zeta_1 \partial \zeta_2} \right\|^2 \right\} d\zeta$$

[1]

$\mathbf{X}_d$ are the measured coordinates and $\mathbf{X}(\xi_d)$ is the interpolated value of ξ_d which is defined by the projection of the measured point onto a surface. The difference field **u** is equal to $\mathbf{X}\text{-}\mathbf{X}^0$ where $\mathbf{X}^0$ is the initial estimate of the shape. Since the HARP analysis doesn't provide information about through plane motion, the data weights, γ_d, were adjusted according to the orientation of the MR slice. Displacement data from short-axis images (Figure 3.5A) were assigned weights of zero in the X direction and data from long-axis images (Figure 3.5B) were assigned zero weights in the Y and Z directions. To regularize the fits, a smoothing function was included. The α and β smoothing weights penalized excessive changes in the first and second derivatives of **u**. An analysis was performed to find the maximal values of the smoothing weights that would not increase the fitting errors significantly beyond the estimated measurement accuracy [101].

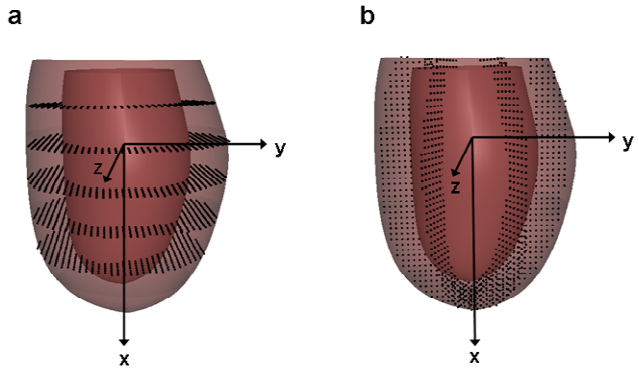

Figure 3.5: Undeformed material points from short axis images (a) and long axis images (b)

3.2.7 Statistics

All measurements are presented as mean ± SD. Student's *t*-test was used to compare end systolic strains, torsion, and geometry measurements between VclKO and WT mice. Strain time courses were compared by two-way repeated measures ANOVA. P values < 0.05 were considered significant.

3.3 Results

3.3.1 Geometric models

A representative WT model at end-diastole is shown in Figure 3.4C with a RMS fitting error of 0.10 mm. From the geometric models, end-diastolic volume (EDV), end-systolic volume (ESV), and ejection fraction (EF) were calculated. In WT mice, EDV = 45 ± 4 ul, ESV = 22 ± 4 ul, and EF = 53 ± 4 %. These values were significantly different in the VclKO mice with EDV = 63 ± 2 ul, ESV = 37 ± 3 ul, and EF = 41 ± 6%. The larger EDV and lower EF in VclKOs indicate ventricular dilation and systolic dysfunction. LV mass was normalized by body mass (LVMI). LVMI was 4.3 ± 0.3 mg/g in VclKOs and 3.9 ± 0.4 mg/g in WT mice. LVMI was significantly higher in VclKO mice, which suggests that there is cardiac hypertrophy. However, lung and liver weights were not significantly different between VclKO and WT mice indicating that the VclKO mice were not in decompensated heart failure.

3.3.2 Fitting error analysis

To find the optimal smoothing weights for the data fitting, α and β were varied over a wide range of values. A representative plot of RMS fitting error for end systole

is shown in Figure 3.6A. When holding α/β constant, the optimal ratio for the lowest error was α/β = 10. This holds for all coordinates as well as VclKO and WT hearts. Figure 3.6B is a box and whisker plot of the variation of RMS error over different α values with α/β = 10. The RMS error begins to increase more rapidly at α = 1. Choosing α to be between 0.1 and 1 allows for the RMS fitting error to be similar to the estimated HARP measurement error of 0.08 pixels which is 0.013 mm [98].

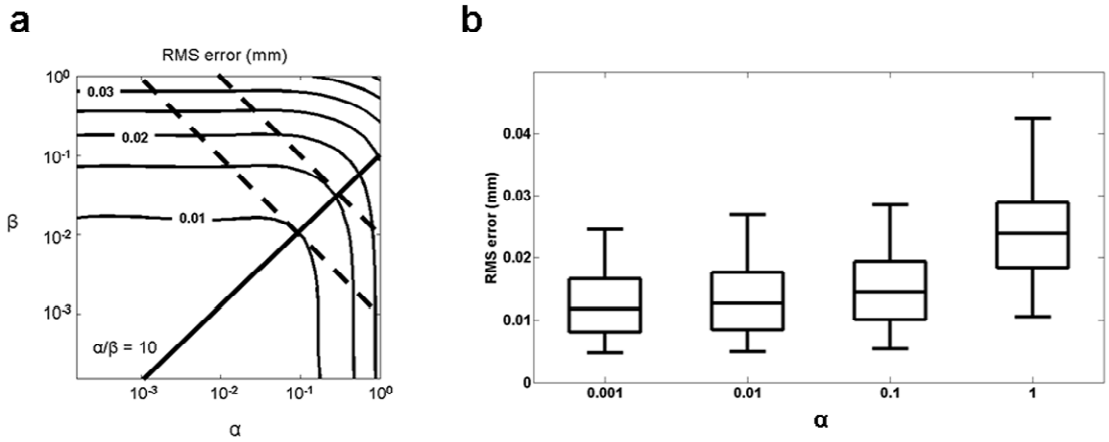

Figure 3.6: RMS error over a range of β and α smoothing weights (a). Keeping α/β constant, the lowest error trajectory falls on the solid line where α/β = 10. RMS error over a range of α weights with α/β = 10 (b)

To validate the accuracy of the deformable model, end-systolic cavity and wall volumes were compared with corresponding volumes from a geometric model created directly from cine MR images at end systole of the same mouse heart (Figure 3.7). Linear regression analysis showed a strong correlation between the ESVs calculated from the deformable model and the MR-derived geometric model (R = 0.94). LV wall volumes were also strongly correlated (R = 0.92).

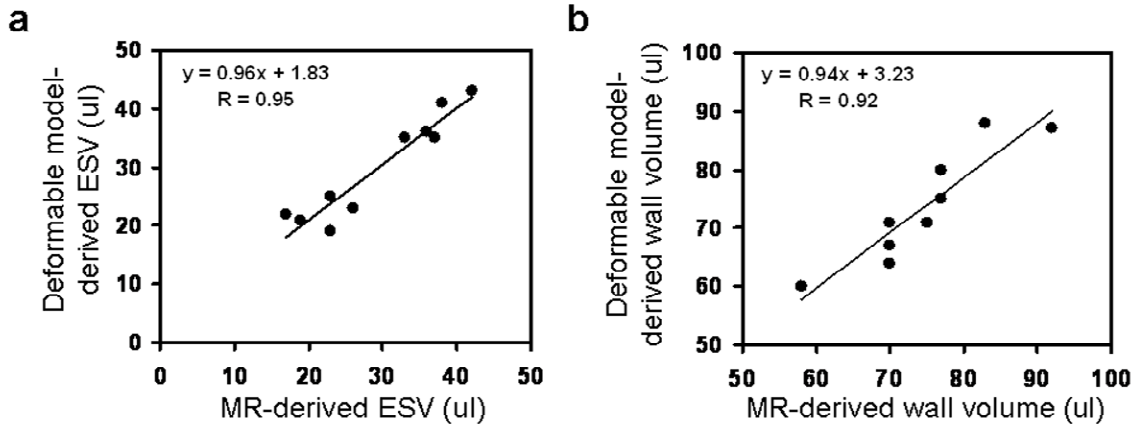

Figure 3.7: Linear regression analysis shows a shows strong correlation between ESV (a) and wall volumes (b) derived from the deformable model and volumes derived from non-tagged MRI.

3.3.3 3D strain analysis

Figure 3.8 shows representative 3D end systolic strain maps from a KO and WT heart. The maps show smoothly varying strain distributions along the posterior LV endocardium and transmurally through the septal and lateral walls. Table 3.1 compares end-systolic strains between VclKO and WT hearts at different transmural locations in the lateral free wall. In WT mice, the radial strain (E_{rr}) was positive which indicates systolic wall thickening. Both the longitudinal and circumferential strains (E_{ll} and E_{cc} respectively) were negative indicating shortening in those directions. The torsional shear (E_{cl}) was positive, consistent with expected right-handed twist, and all shear components were non-zero. In VclKOs, E_{rr} was significantly lower than in WT mice at the endocardium in the mid-ventricle and apex, indicating reduced systolic wall thickening in these regions. In Figure 3.9, the average E_{rr} in several transmural segments of the lateral wall are plotted for representative WT and VclKO hearts. In the

WT heart, there is a transmural E_{rr} gradient which is diminished in the VclKO hearts. The E_{cr} transverse shear was also significantly lower in the apical wall, and the torsional shear (E_{cl}) was significantly lower in the mid ventricle. From the deformable models, peak torsion was 40 ± 6 degrees/cm in WT hearts. Peak torsion in VclKOs was 25 ± 6 degrees/cm and significantly lower than WT values.

Table 3.1: 3D Lagrangian strain tensor components in the LV lateral wall of WT and VclKO hearts

		Base			**Mid Ventricle**			**Apex**		
		Endo	*Mid*	*epi*	*Endo*	*mid*	*epi*	*endo*	*mid*	*epi*
E_{cc}	*WT*	-0.13 ± 0.05	-0.07 ± 0.02	-0.05 ± 0.01	-0.17 ± 0.03	-0.12 ± 0.05	-0.10 ± 0.04	-0.17 ± 0.06	-0.12 ± 0.07	-0.09 ± 0.05
	KO	-0.11 ± 0.04	-0.09 ± 0.02	-0.06 ± 0.02	-0.13 ± 0.05	-0.12 ± 0.03	-0.09 ± 0.02	-0.16 ± 0.05	-0.13 ± 0.02	-0.09 ± 0.02
E_{ll}	*WT*	-0.13 ± 0.04	-0.13 ± 0.04	-0.11 ± 0.05	-0.13 ± 0.05	-0.13 ± 0.04	-0.12 ± 0.03	-0.17 ± 0.04	-0.16 ± 0.04	-0.15 ± 0.05
	KO	-0.09 ± 0.03	-0.10 ± 0.03	-0.09 ± 0.03	-0.13 ± 0.02	-0.12 ± 0.02	-0.11 ± 0.03	-0.13 ± 0.02*	-0.12 ± 0.01	-0.10 ± 0.01
E_{rr}	*WT*	0.25 ± 0.11	0.19 ± 0.08	0.10 ± 0.04	0.39 ± 0.15	0.25 ± 0.13	0.12 ± 0.09	0.20 ± 0.07	0.15 ± 0.05	0.11 ± 0.04
	KO	0.13 ± 0.07	0.14 ± 0.09	0.09 ± 0.07	0.09 ± 0.03*****	0.12 ± 0.05	0.13 ± 0.09	0.09 ± 0.06*	0.12 ± 0.07	0.14 ± 0.08
E_{cl}	*WT*	0.02 ± 0.01	0.03 ± 0.02	0.02 ± 0.01	0.05 ± 0.02	0.05 ± 0.02	0.05 ± 0.01	0.02 ± 0.03	0.02 ± 0.02	0.01 ± 0.02
	KO	0.01 ± 0.02	0.02 ± 0.02	0.01 ± 0.01	0.02 ± 0.01*	0.03 ± 0.02	0.02 ± 0.02*	0.02 ± 0.01	0.01 ± 0.01	0.00 ± 0.01
E_{cr}	*WT*	-0.06 ± 0.06	-0.07 ± 0.07	-0.10 ± 0.09	0.00 ± 0.05	0.01 ± 0.03	0.00 ± 0.02	0.07 ± 0.04	0.10 ± 0.04	0.05 ± 0.05
	KO	-0.01 ± 0.03	-0.05 ± 0.07	-0.06 ± 0.07	0.00 ± 0.05	-0.03 ± 0.03	-0.05 ± 0.06	0.01 ± 0.03*	0.01 ± 0.03*	0.01 ± 0.04
E_{lr}	*WT*	0.07 ± 0.10	0.05 ± 0.10	-0.01 ± 0.07	-0.01 ± 0.03	-0.02 ± 0.03	0.00 ± 0.02	-0.04 ± 0.02	-0.02 ± 0.03	-0.02 ± 0.02
	KO	0.02 ± 0.08	0.02 ± 0.07	0.01 ± 0.06	-0.01 ± 0.03	-0.01 ± 0.03	-0.13 ± 0.02	-0.05 ± 0.03	-0.02 ± 0.02	0.01 ± 0.02

* $P < 0.05$ between KO and WT

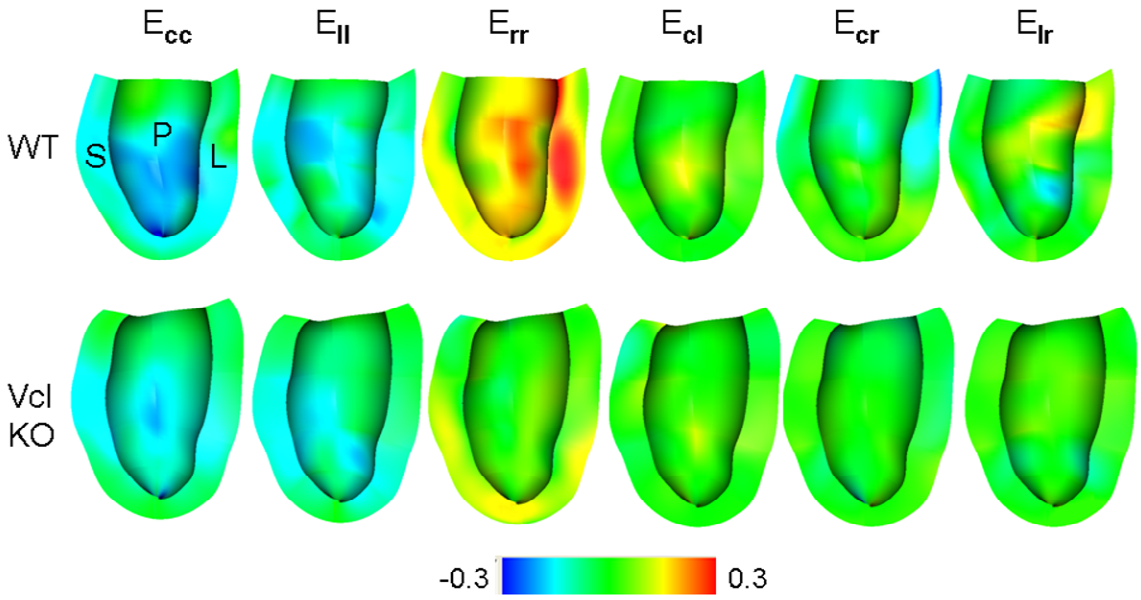

Figure 3.8: 3D end-systolic strain maps of the LV in representative WT and VclKO hearts. Transmural strain distributions are shown at the septal (S) and lateral wall (L). Endocardial strains are displayed on the posterior wall (P). The strain tensor components shown are circumferential strain (E_{cc}) , longitudinal strain (E_{ll}), radial strain (E_{rr}), torsional shear (E_{cl}), and the transverse shears(E_{cr}, E_{lr})

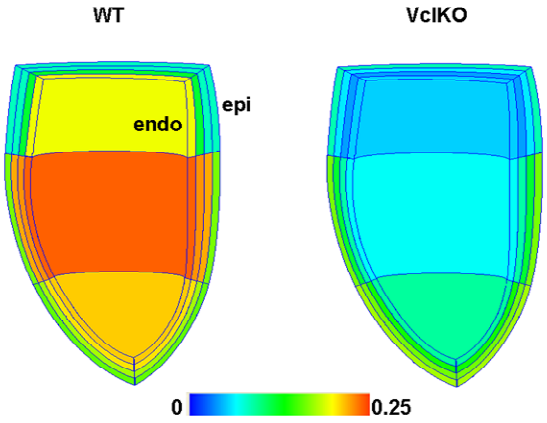

Figure 3.9: Average end-systolic radial strains in transmural segments of the lateral wall of WT and KO hearts.

Strain distributions were also calculated throughout the cardiac cycle to examine differences in the temporal development of strain. Strain time courses in the ventricular lateral wall at the endocardium are shown in Figure 3.10. Time courses for radial strain and torsional shear were found to be significantly different between VclKO and WT hearts with $P < 0.05$.

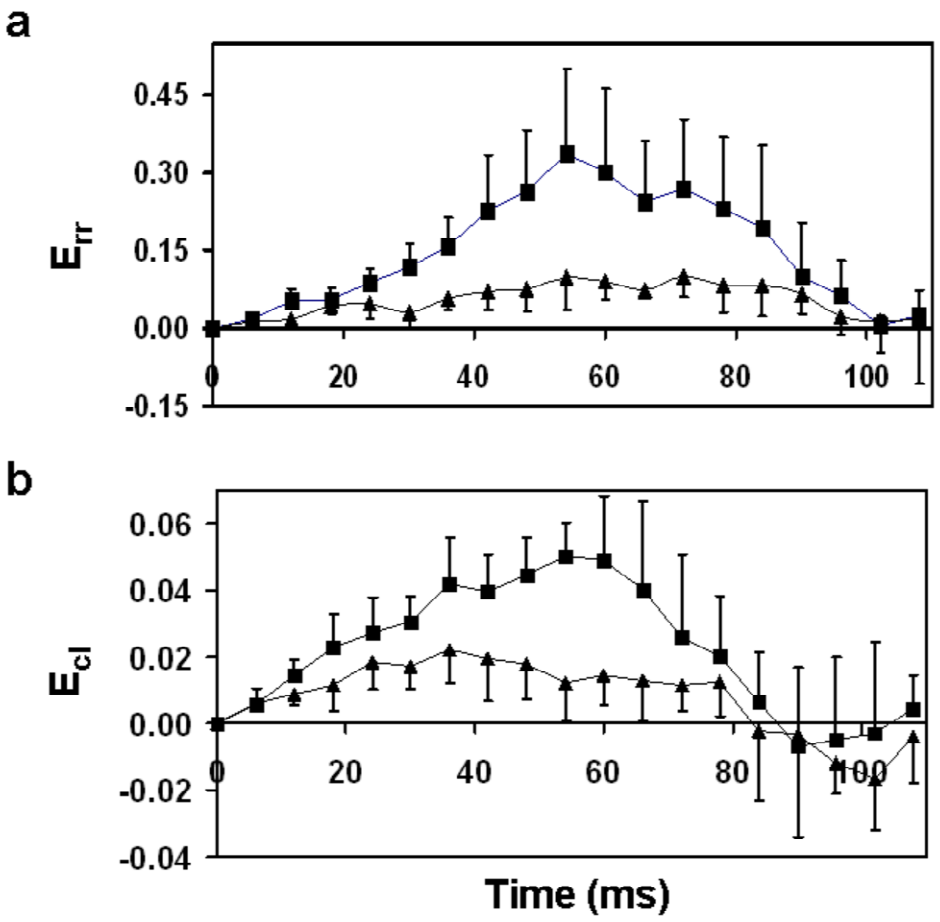

Figure 3.10: Comparison of WT (■) and VclKO (▲) strain time courses for E_{rr} (a) and E_{cl} (b) in the endocardium of the lateral wall.

3.4 Discussion

In previous mouse MR tagging studies, either HARP or finite element modeling have been used separately to help calculate 3D strains in the heart. In this study, we combined the strengths of HARP and finite element modeling for a more efficient and accurate 3D strain analysis of the mouse heart. HARP was used to facilitate material point tracking. Unlike manual tracing of taglines, HARP allows for automatic point tracking, which greatly reduces processing time. Errors in tracking sometimes occur near the edges of the myocardium, but these points are easily removed from the analysis. Strain measurements are also not restricted by tag line resolution since displacement data from every pixel in the myocardium can be used. Sub-pixel resolution in point tracking also allows for more precision in displacement measurements. The HARP analysis could have been improved with the use of CSPAMM pulse sequence, which reduces artifacts by suppressing the central peak in k-space [102]. However, implementation of CSPAMM requires twice the number of image acquisitions, which would increase scan time and costs significantly. HARP analysis also assumes that there are small tissue deformations from one time frame to the next; therefore, it may fail when there are large tissue deformations. With HARP, it is assumed that the tag spacing and orientation do not change with reference to the end-diastolic state. Gabor filters can provide for more robust point tracking. The Gabor filter can be adjusted to correspond with the local tag spacing and orientation which results in more accurate phase maps of the deformed tissue [103].

With a deformable finite element model, 3D strain distributions were calculated throughout the LV wall. Unlike homogenous strain analysis, the strain fields produced from finite element modeling were nonhomogenous and smooth. They could be reconstructed with sufficient sensitivity to detect of variations in deformation by region and genotype. The addition of smoothing weights to the data fitting reduced the model's susceptibility to noise. By systematically varying the smoothing weights, the optimal values were found such that the RMS error was similar to the magnitude of the measurement error while minimizing the strain energy of the resulting deformations. The model was also able to reproduce global changes in geometry. End-systolic geometry of the deformable model agreed well with measurements made from end-systolic untagged cine images. The use of finite element strain analysis with MR tagging has also been validated in large animals and gel phantoms [104].

The geometric models made from the cine MR images allow for the incorporation of accurate cardiac geometries, which is important since diseased hearts are usually abnormal in shape and size. Fitting of the LV geometry from cine MR data and measurement of wall and cavity volumes has been previously validated by us [105,106]. EDV and EF calculated from the geometries in the WT mice were close to the ranges reported in literature [65,70,85,107]. Slight differences may be attributed to background strain, age, and anesthesia levels. Previously published results from echocardiography and histology show that the VclKO hearts have dilation, hypertrophy, and decreased fractional shortening [62]. The EDV, EF, and LVMI values calculated from MRI were consistent with these previous findings.

The 3D end-systolic strain patterns calculated in the WT lateral free wall agree well with previously published mouse data in terms of magnitude and sign [94,95]. Base-to-apex strain variations, such as E_{cr} transitioning from negative (base) to positive (apex), are found to be similar [94]. The WT data shows that E_{rr} is generally larger at the endocardium than the epicardium. This transmural gradient in radial strain is consistent with data published from large animal studies [108,109] and in mice [85]. Torsion measurements are also similar to values found in literature for the mouse heart [82].

End-systolic stains in the VclKO hearts showed patterns characteristic of human cases of DCM. In human patients with DCM, radial wall thickening and peak torsion are reduced [110-112]. Circumferential and longitudinal shortening in the lateral wall are relatively unchanged from levels found in healthy subjects [110]. In the VclKO hearts, E_{rr} is significantly lower in the endocardium compared to WT levels. Torsional shear and torsion were decreased in VclKO mice as well. E_{cc} and E_{ll} were not significantly different from WT values across the majority of the lateral free wall.

In summary, the current technique combines SPAMM tagging, HARP tracking, and finite element modeling to calculate 3D finite strain distributions in the mouse LV. The technique is capable of distinguishing abnormal 3D strain patterns in different mouse models of cardiovascular disease. In this study, 3D strains were only presented in cardiac coordinates. However, this computational approach provides a convenient framework for the inclusion of fiber architecture and the measurement of fiber and sheet strains. Myocardial material properties can also be estimated with the appropriate

pressure measurements, which may provide further insight into the origin and progression of different cardiovascular diseases.

Chapter 3, in part, was submitted to the *Journal of Magnetic Resonance in Medicine*, with authors Chuang JS, Zemlijic-Harpf A, Ross RS, Frank LR, McCulloch AD, and Omens JH. The dissertation author is the primary investigator and author of this material.

4 The role of vinculin in regional sheet and fiber ventricular mechanics

4.1 Introduction

The 3D structure of the heart involves fiber and sheet structures, which play important roles in cardiac function. Myofibril orientation varies from about –60º at the epicardium to +60º at the endocardium. The fibers are arranged into branching laminar sheets, which are about 4 cells thick [31]. Fibers within a sheet are tightly coupled by endomysial collagen struts that connect adjacent cardiomyocytes at their costameres. The sheets are covered by a network of perimysial collagen, and adjacent sheets are loosely coupled by long perimysial collagen strands. The fiber and sheet structures can be used to define a local material coordinate system (Figure 4.1). The fiber axis, X_f, is obtained by a rotation about radial axis through the fiber angle. Another rotation about

X_f through the sheet angle gives the sheet axis, X_s, which lies in the sheet plane and is normal to X_f. The cross product of X_f and X_s yields the sheet normal axis, X_n.

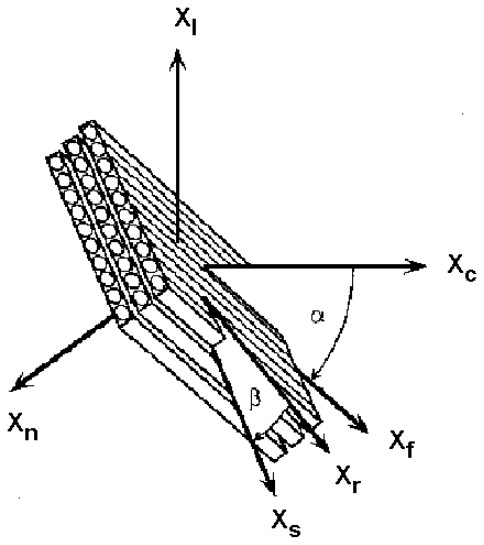

Figure 4.1: Fiber and sheet coordinate system.

This higher order sheet structure is thought to provide the basis for the rearrangement of cardiomyocytes during systolic ventricular thickening [33]. During systole, radial thickening of the LV wall is important for the ejection of blood from the ventricle [113]. Myocardial sheets contribute to ventricular wall thickening through lengthening of the sheets transverse to the fibers (E_{ss}). Within a sheet, the tight coupling between costameres of adjacent cells allows for force transmission through the sheet. During systole, interlaminar shear (E_{sn}) also occurs such that adjacent sheets slide against each other parallel to the sheet direction and orient more radially [33]. The loose coupling of adjacent sheets by perimysial collagen allows for large shearing deformations. The fiber and laminar structures are also important during diastole. Early diastolic relaxation involves dynamic fiber-sheet mechanics characterized by

stretch along the myofibers at the epicardium of the LV myocardium, shortening in the sheet plane transverse to the myofibers in the endocardium, and shearing in the sheet plane [35,36]. The deformations of the fiber and sheet structures may help torsional recoil and early diastolic filling [35,36].

Interlaminar shear results from the sliding of adjacent myocardial sheets, which depends on the long perimysial collagen fibers and not necessarily the cell-ECM connections. However, sheet strain represents deformation within a sheet and may be directly related to the cell-ECM linkages. Endomysial collagen struts link costameres of adjacent cells together in the transverse direction and play an important role in force transmission in the sheet direction. Thus, weakening of the ECM-cell interactions through Vcl deletion may directly affect mechanics within the sheet and in the sheet direction. We hypothesize that Vcl deletion will alter systolic sheet strain prior to the onset of heart failure. In this study, we examined the effect of Vcl deletion on regional fiber/sheet mechanics in the mouse heart prior to the onset of heart failure.

Three-dimensional cardiac strains were measured *in vivo* with MR tagging (as described in Chapter 3). The fiber and sheet orientations were obtained from histological measurements to calculate 3D strains in the fiber and sheet coordinates. In VclKO mice, there was a decrease in end-systolic sheet extension which decreased radial strain. The decrease in wall thickening may be responsible for the measured reduction in interlaminar shear. Fiber strains remained unchanged which indicated that Vcl deletion did not interfere with the cardiomyocyte's ability to contract.

4.2 Methods

4.2.1 Mice

Six week-old male VclKO mice (n = 5) and WT littermates (n = 5) with no Vcl excision were used for the MRI study. All protocols were performed according to the National Institutes of Health's *Guide for the Care and Use of Laboratory Animals* and approved by the UCSD Animal Subjects Committee.

4.2.2 MRI

Cine and SPAMM tagging were performed as described in section 3.3.3.

4.2.3 Geometric model

Anatomical models of mouse LVs were created as described in section 3.3.5.

4.2.4 Histology

After imaging, the mouse hearts were arrested with a hyperkalemic solution and fixed with 10% buffered formalin. Each heart was cut into three pieces for fiber and sheet angle measurement. Each tissue piece was embedded in OCT and cryosectioned to produce 10 μm slices. The first block was sectioned through the LV free wall parallel to the epicardial circumferential-longitudinal plane (1-2) for transmural fiber angles (α). A continuous fiber angle distribution through the wall was calculated by a linear least squares fit of the measured α. The remaining tissue pieces were sectioned parallel to the circumferential radial (1-3) plane or the longitudinal-radial (2-3) surface. Cleavage plane angles β'' and β' were measured from the 1-3 and 2-3 surfaces

respectively. Sheet angles (β) were calculated at different transmural depths with the following equations [33]:

$$\beta_{2\text{-}3} = \arctan(\cos\alpha \tan\beta') \quad [1a]$$

$$\beta_{1\text{-}3} = \arctan(-\sin\alpha \tan\beta'') \quad [1b]$$

Two different distributions, $\beta_{2\text{-}3}$ and $\beta_{1\text{-}3}$, were obtained from Eqn. 1a and 1b. These equations take into account the effect of the fiber angle on the theoretical accuracy of the cleavage-plane angle measurement. To approximate β from these two distributions, the following equation was used:

$$\beta = (\cos^2\alpha)(\beta_{2\text{-}3}) + (\sin^2\alpha)(\beta_{1\text{-}3}) \quad [2]$$

4.2.5 Fiber and sheet strains

The 3D strain tensor in cardiac coordinates was calculated as described in section 3.3.6. To calculate strains in the fiber and sheet coordinate system, the cardiac strain tensor was transformed with the following equations:

$$M = \begin{bmatrix} Cos\alpha & Sin\alpha & 0 \\ -Sin\alpha Sin\beta & Cos\alpha Sin\beta & Cos\beta \\ Sin\alpha Cos\beta & -Cos\alpha Cos\beta & Sin\beta \end{bmatrix} \quad [3a]$$

$$\begin{bmatrix} Eff & Efs & Efn \\ Efs & Ess & Esn \\ Efn & Esn & Enn \end{bmatrix} = M \begin{bmatrix} Ecc & Ecl & Ecr \\ Ecl & Ell & Elr \\ Ecr & Elr & Err \end{bmatrix} M^T \quad [3b]$$

Cardiac strain tensors were transformed using fiber and sheet angles from the same mouse heart.

4.2.6 Statistics

All measurements are presented as mean ± SD. Student's *t*-test was used to compare end systolic strains, and geometry measurements between VclKO and WT mice. Fiber angles, sheet angles, and strain time courses were compared by two-way repeated measures ANOVA. P values < 0.05 were considered significant.

4.3 Results

4.3.1 Global geometry and function

From the geometric models, EDV, ESV, EF, and LVMI were measured. Table 4.1 compares these values between the 6 wk old VclKO and WT mice. EDV and ESV were slightly larger in VclKO, but not significantly different. There were also no significant differences in EF and LVMI between VclKO and WT mice. VclKO lung and liver weights were within the normal range.

Table 4.1: Global geometry and function in 6wk old VclKO and WT mice

Mouse	EDV(ul)	ESV(ul)	EF(%)	LVMI (mg/g)
WT	43 ± 2	17 ± 4	60 ± 9	3.8 ± 0.2
VclKO	50 ± 11	25 ± 6	50 ± 4	4.1 ± 0.7

4.3.2 Fiber and sheet angles

Transmural fiber angles at the equator of the LV free wall were calculated. Figure 4.2 shows the linear distribution of α for VclKO and WT hearts. There is no significant difference in α between VclKO and WT hearts at this location. The fiber

angles varied linearly from negative values at the epicardium to positive values at the endocardium as expected.

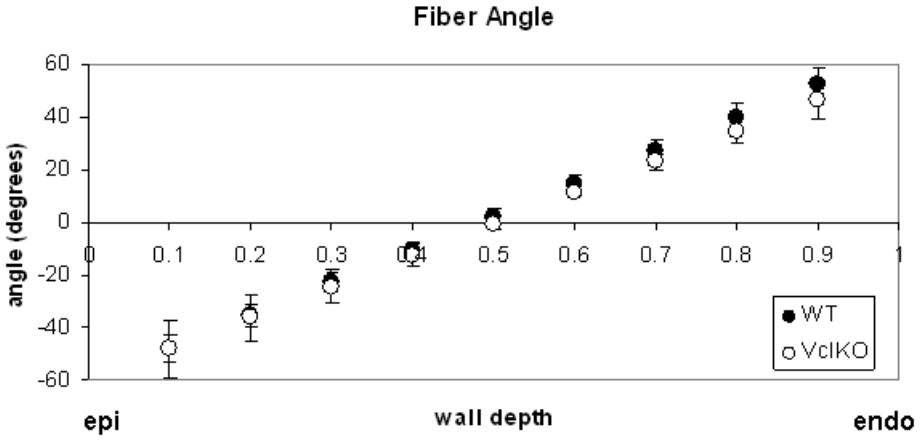

Figure 4.2: Comparison of WT and VclKO transmural fiber angle distributions.

Sheet angles are plotted in Figure 4.3 for VclKO and WT hearts. Sheet angles were on average negative throughout the wall at the mid ventricle. There was no significant difference in sheet angle distribution between VclKO and WT hearts.

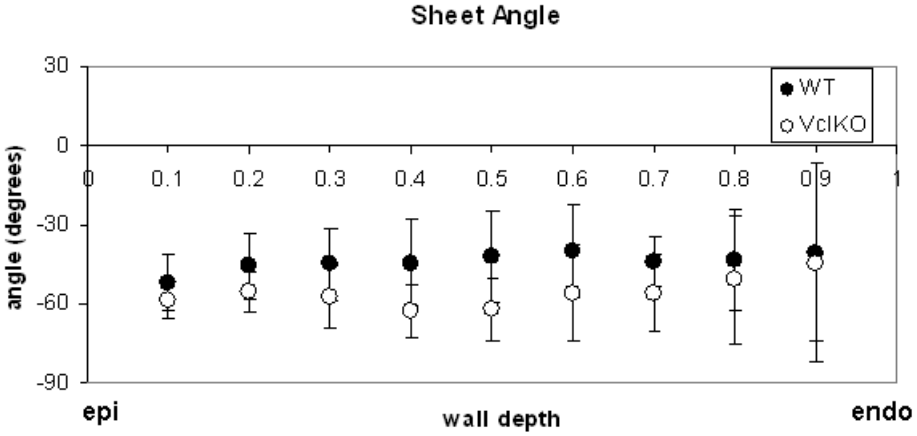

Figure 4.3: Comparison of WT and VclKO transmural sheet angle distributions.

4.3.3 Cardiac strains

Figure 4.4 compares transmural end-systolic normal strains between 6 week old VclKO and WT hearts at the equator of the LV lateral free wall.

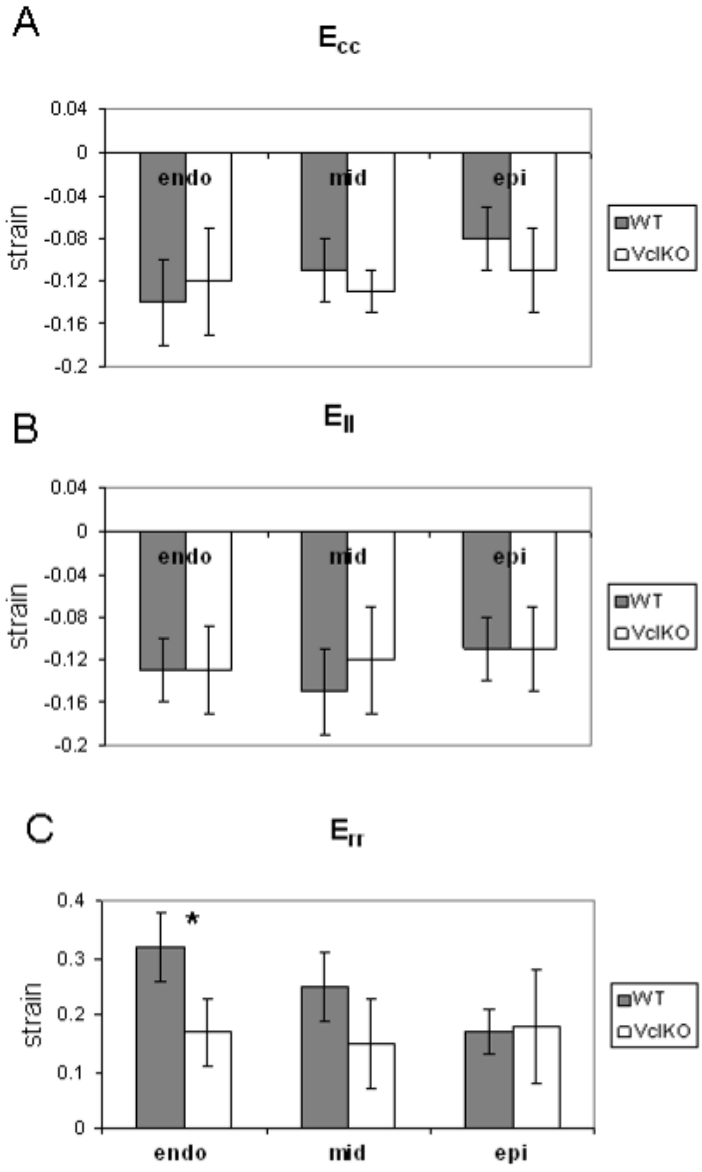

Figure 4.4: Comparison of end-systolic (A) E_{cc}, (B) E_{ll}, (C) E_{rr}. In the VclKO, E_{rr} was significantly lower in the endocardium ($P < 0.05$).

In WT mice, the radial strain (E_{rr}) was positive which indicates systolic wall thickening. Both longitudinal and circumferential strains (E_{ll} and E_{cc} respectively) were negative indicating shortening in those directions. In VclKOs, E_{rr} was significantly lower in the endocardium, indicating reduced wall thickening.

Figure 4.5 compares transmural end-systolic shear strains between 6 week old VclKO and WT hearts at the equator of the LV lateral free wall.

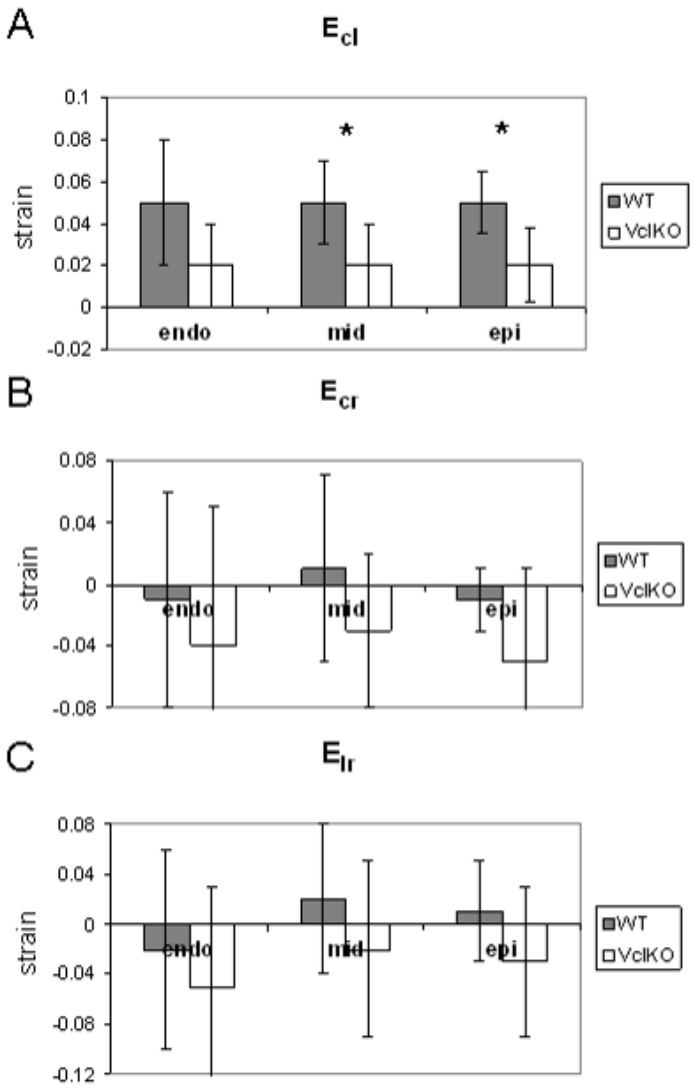

Figure 4.5: Comparison of end-systolic (A) E_{cl}, (B) E_{cr}, (C) E_{lr}. In the VclKOs, E_{cl} was significantly lower in the mid-wall and epicardium ($P < 0.05$).

In WT mice, the torsional shear (E_{cl}) was positive and consistent with the expected right-handed twist. The torsional shear (E_{cl}) was significantly lower in the mid-wall and epicardium of VclKO hearts. There were no other significant differences between WT and VclKO shear strains.

Cardiac strain distributions were also calculated throughout the cardiac cycle to examine differences in the temporal development of strain. Figure 4.6 shows the radial strain time course in the lateral free wall at the endocardium. The radial strain time course was found to be significantly different between VclKO and WT hearts. In the VclKO heart, there was a decrease in radial thickening.

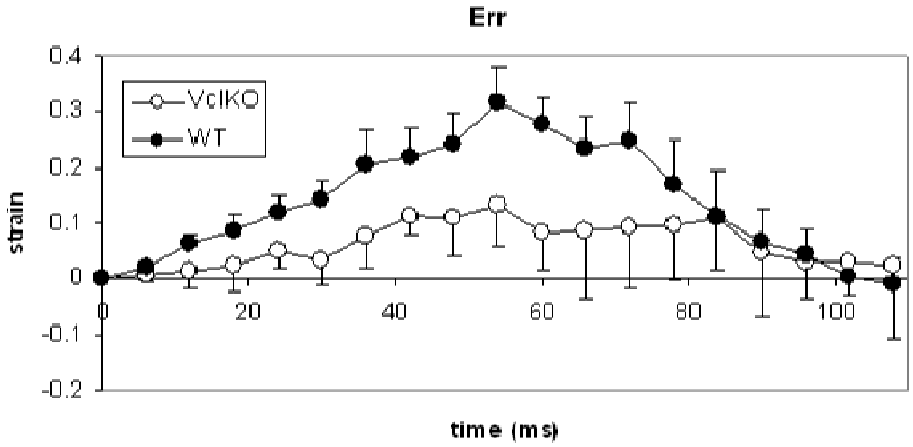

Figure 4.6: The E_{rr} time course was significantly different in the endocardium of the lateral wall between VclKO and WT hearts.

4.3.4 Fiber and sheet strains

Cardiac strains were transformed into fiber-sheet coordinates. End-systolic fiber-sheet normal strains are shown in Figure 4.7. In WT mice, the fiber strain (E_{ff}) was negative which indicates fiber shortening and was fairly uniform throughout the

wall. E_{ss} was positive indicating lengthening in the sheet axis direction. In VclKOs, E_{ss} was significantly lower than in WT mice at the endocardium and mid-wall, indicating reduced sheet extension. No significant differences were found between WT and VclKOs with the other normal strains.

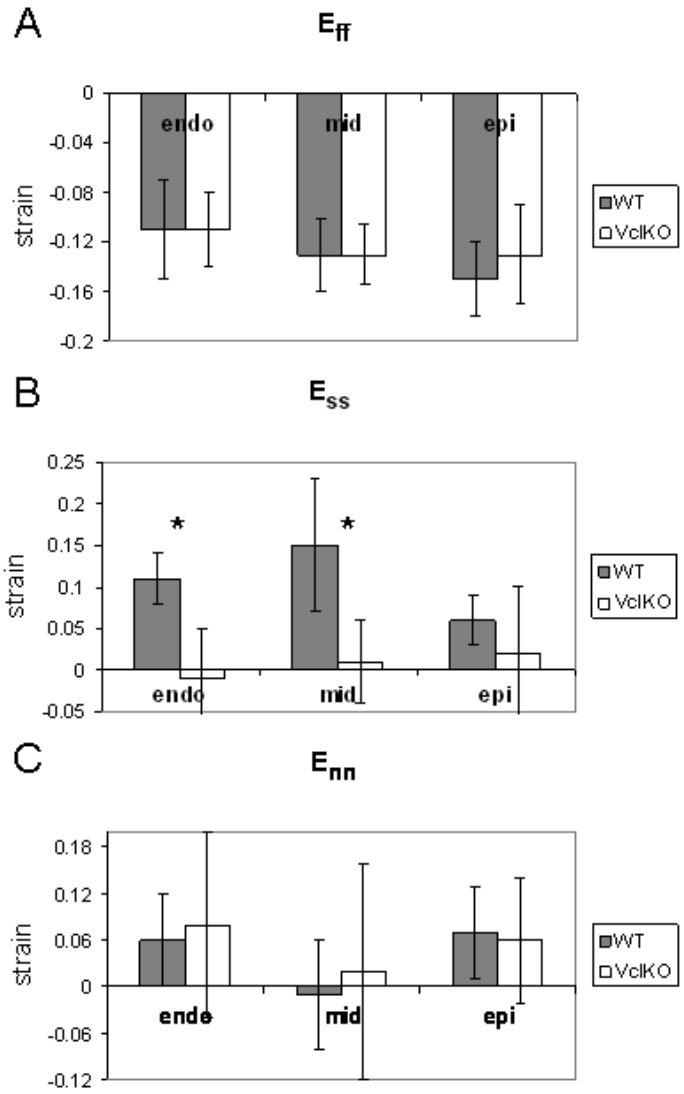

Figure 4.7: Comparison of end-systolic (A) E_{ff}, (B) E_{ss}, (C) E_{nn}. In the VclKO, E_{ss} was significantly lower in the endocardium and mid-wall ($P < 0.05$).

Figure 4.8 compares transmural end-systolic fiber/sheet shear strains between VclKO and WT hearts at the equator of the LV lateral free wall. In the WT hearts, E_{sn} was consistently negative, which contributed to wall thickening. In the VclKO hearts, E_{sn} was significantly smaller in magnitude at the endocardium. No significant differences were found between WT and VclKOs with the other shear strains.

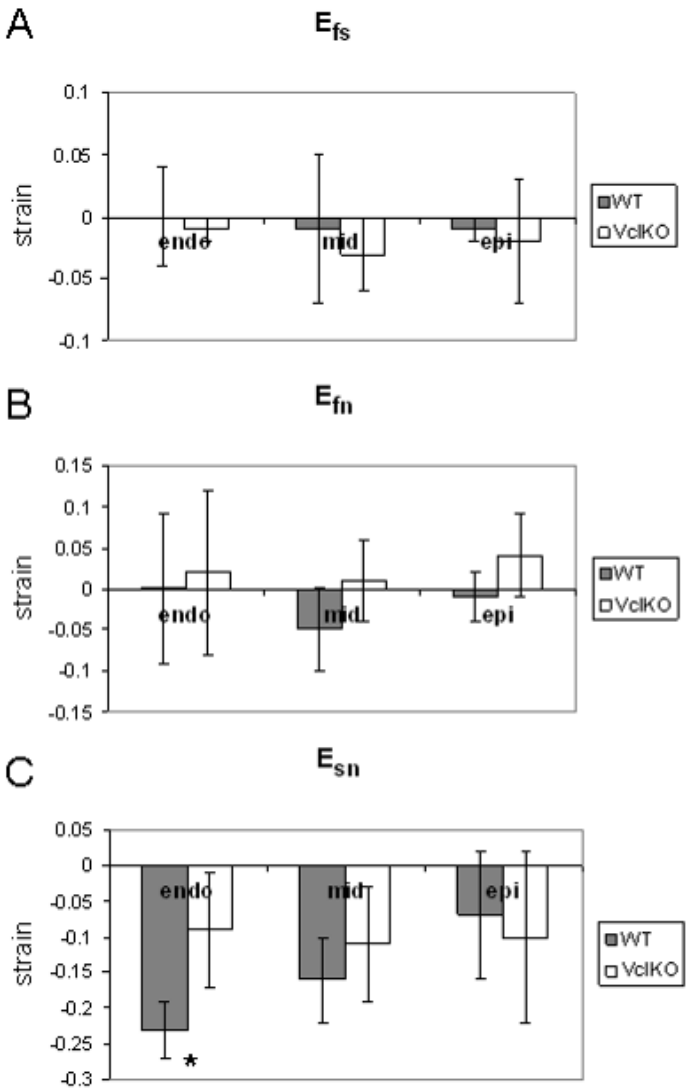

Figure 4.8: Comparison of end-systolic (A) E_{fs}, (B) E_{fn}, (C) E_{sn}. In the VclKO, E_{sn} was significantly smaller in magnitude at the endocardium ($P < 0.05$).

Fiber-sheet strain distributions were also calculated throughout the cardiac cycle to examine differences in the temporal development of strain. Strain time courses in the lateral free wall at the endocardium are shown in Figure 4.9. Time courses for E_{ss} and E_{sn} were found to be significantly different between VclKO and WT hearts.

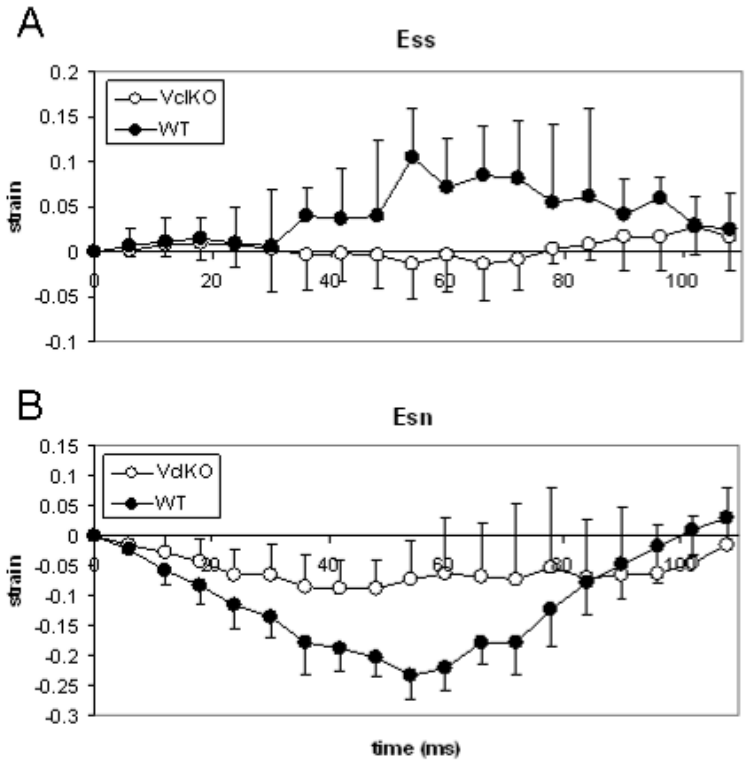

Figure 4.9: Comparison of WT and VclKO strain time courses for E_{ss} (A), and E_{sn} (B) in the endocardium of the lateral free wall.

4.4 Discussion

In this study, we examined the effect of Vcl deletion on regional fiber/sheet mechanics in the mouse heart prior to the onset of heart failure. VclKO mice were studied at a younger age before the onset of cardiac dysfunction. EDV and EF

calculated from the geometries in the WT mice were close to the ranges reported in literature [65,70,85,107]. Slight differences may be attributed to background strain, age, and anesthesia levels. On average, 6 week old VclKO hearts were slightly larger than WT hearts and ejection fraction was lower, but there were no significant differences detected. LVMI was not significantly different between VclKO and WT hearts, so no hypertrophy was present at that age. Thus, at 6 weeks of age no significant differences were detected in global function of the VclKO heart, but ejection fraction may have just begun to decrease with an increase in LV chamber size.

The 3D end-systolic strain patterns calculated in the WT lateral free wall agree well with previously published mouse data in terms of magnitude and sign [94,95]. In previously published data, average end-systolic $E_{rr} = 0.30 \pm 0.15$, $E_{ll} = -0.12 \pm 0.03$, $E_{cc} = -0.10 \pm 0.03$, and $E_{cl} = 0.05 \pm 0.01$ [94]. Our WT data shows that E_{rr} is positive, indicating systolic wall thickening, and generally larger at the endocardium than the epicardium. At the endocardium, E_{rr} equals 0.32 ± 0.06, which is close in magnitude to previously published data. Both E_{ll} and E_{cc} in the WT heart were negative indicating shortening in those directions. The torsional shear ($E_{cl} \approx 0.05$) was positive and smaller in magnitude than the normal strains, which was consistent with previously published data. In VclKOs, E_{rr} was significantly lower than in WT mice at the endocardium, indicating reduced systolic wall thickening, and the torsional shear (E_{cl}) was significantly lower in the mid-wall and epicardium. Cardiac strain time courses also showed that development of radial strain was significantly different in the VclKO heart.

In order to calculate strains in the fiber/sheet coordinates, histology was used to measure fiber and sheet orientations. Fiber angles showed the normal transition from approximately -60 at the epicardium to 60 degrees at the endocardium. Sheet angles were generally negative throughout the wall and were similar to previously published mouse data [114]. Vcl deletion from the myocardium did not seem to change sheet or fiber orientation. Measurement of the fiber and sheet orientations with histology was a labor intensive and time consuming process, so angles were only measured in one location. Diffusion tensor MRI (DTI) has also been used to facilitate and improve the fiber and sheet measurements. With diffusion weighted spin echo sequences, the entire heart can be scanned and the diffusion tensor calculated throughout the ventricle [115]. Since water diffuses more readily down the axis of the myocyte versus any cross sectional direction, the primary eigenvector would be interpreted as being parallel to the fiber direction. The secondary eigenvector would give the sheet direction of the myocardial laminae and the tertiary eigenvector would be the normal direction of the sheet structure [115]. DTI allows for measurement of the fiber and sheet structures and thus strains throughout the entire heart instead of at just one location.

With the fiber and sheet orientations, cardiac strains were transformed into the fiber/sheet coordinate system. Strain magnitudes and signs in WT mice corresponded to some of the values measured in large animal studies [33,109]. In dog hearts, fiber shortening (E_{ff} = -0.07 ± 0.04), sheet lengthening (E_{ss} = -0.11 ± 0.08), and interlaminar shear (E_{sn} = -0.07 ± 0.09) were measured during systole [33]. In the WT mice, E_{ff} was negative and E_{ss} was positive, indicating fiber contraction and sheet extension

respectively. E_{sn} shear was negative; thereby contributing to wall thickening. E_{ss} was similar in magnitude to the dog data; however, E_{ff} and E_{sn} were slightly larger in magnitude compared to the dog strains. In VclKO mouse hearts, end-systolic E_{ff} strain was not significantly different from WT hearts. In the VclKO heart, sheet strain and interlaminar shear (E_{ss} and E_{sn} respectively) were both smaller in magnitude than in the WT heart. E_{ss} and E_{sn} normally contribute substantially to wall thickening, particularly in the endocardium. In the VclKO heart, the decrease in magnitude of E_{ss} may lead to a decrease in radial thickening (E_{rr}). Decreased wall thickening may restrict relative movements of sheet and reduce E_{sn}.

In these younger VclKO hearts, cardiomyocytes are able to contract normally since end-systolic E_{ff} is unchanged. However, the 3D integrated movement involving larger sheet structures is changed. Within the laminar sheet, adjacent cardiomyocytes are coupled tightly together by an endomysial collagen network [31]. E_{fs} (shear within the sheet plane) was small in both WT and VclKO hearts indicating that cardiomyocytes remain parallel to neighboring cells and do not slide past each other during systole. The extensive array of endomysial collagen struts surrounding the cells may prevent shearing within the sheet. Shear within the sheet was not affected by Vcl deletion; however, sheet extension was decreased. Sheet extension in the normal heart may occur as a result of myocyte rearrangement within the sheet. The endomysial collagen network limits slippage and shearing of cells within a sheet, but it permits reversible interdigitation of cells which may be the mechanism responsible for sheet lengthening during systole [116]. In VclKOs, there may be an increased number of

collagen struts in order to compensate for weakening of the costameres. Collagen struts are transverse to the fiber axis, and an increase in their quantity may increase stiffness in sheet direction and limit cellular interdigitation and sheet strain.

Laminar bundles of cells are surrounded by long perimysial collagen fibers which allow for the large interlaminar shears and sheet rearrangement (E_{sn}). During systole, sheets become aligned more radially and contribute to wall thickening. In VclKO hearts, the decrease in E_{sn} may also be the result of an increase of perimysial collagen fibers which makes it more difficult for sheets to slide past each other.

Some interesting changes were seen in VclKO ventricular mechanics when strains were transformed into the fiber/sheet coordinates, but the mechanisms in which sheet mechanics were altered are currently unknown. Collagen staining/quantification as well as scanning electron microscopic examination of extracellular matrix structure may help determine why sheet strains and shears were affected by Vcl deletion.

5 The role of vinculin in passive material properties of myocardium

5.1 Introduction

Passive material properties of myocardium play an important role in ventricular mechanics. Titin is largely responsible for the passive stiffness of the myocardium at lower strains [23]. It is one of the most abundant proteins of the intrasarcomeric cytoskeleton and has multiple functions that contribute to myocardial mechanics [117]. Titin molecules are anchored at the Z-disc and extend to the M-line of the sarcomere [24]. When sarcomeres are stretched, the extension of titin's I-band gives rise to passive force like a molecular spring [118]. During systolic contraction, sarcomeres are shortened below slack length and the compression of titin's I-band creates the restoring force that pushes z-discs to their slack positions. In addition to titin, the extracellular matrix contributes to myocardial passive stiffness. Collagen composes most of the

extracellular matrix of cardiac muscle. In papillary muscles, coiled perimysial collagen strands are oriented parallel to the fiber axis and contribute to the passive tension of myocardial tissue at longer sarcomere lengths [119].

Changes in myocardial stiffness occur for a variety of reasons. Ventricular stiffness can increase in failing myocardium, which results in decreased chamber filling, a higher end diastolic pressure, and lower stroke volume [120]. Some changes in myocardial stiffness are a result of tissue remodeling. Chronic ventricular hypertrophy and fibrosis which are associated with heart failure can increase myocardial stiffness. However, passive material properties can also be altered directly by the deletion of a particular protein. When MLP, a Z-disc protein, is deleted from the mouse heart, the myocardial compliance is higher compared to WT tissue [121]. These changes were observed at 2 weeks of age before the onset of DCM. Therefore, progression to DCM may be initiated by diastolic dysfunction in the MLPKO heart where decreased passive stiffness of the myocardium contributes to ventricular dilation.

In non-cardiac cells where Vcl was deleted, the integrin-cytoskeletal linkages were found to be less stiff using magnetic tweezers and RGD coated beads [58]. Vcl is an actin binding protein that bundles actin filaments [17]. In Vcl null cells, there was also a decrease in actin stress fiber formation [122]. Reorganization of cytoskeletal actin may be responsible for an overall decrease in the stiffness of Vcl null cells as measured by AFM [122].

By weakening critical connections in the myocardium, we hypothesize that Vcl deletion will alter passive material properties. Vcl deletion may disrupt the normal

force transmission pathways from ECM to cytoskeleton through the integrin-based costamere or cell-to-cell force transmission along the myocyte axis, which may manifest as altered passive stiffness. To test the mechanical properties of myocardial tissue, murine RV papillary muscles of Vcl deficient hearts were strained in the axial direction while simultaneously measuring force. Stress-strain curves were significantly different between WT and Vcl deficient papillary muscles, and Vcl deficient muscles were found to be more compliant. The study shows that Vcl contributes to the passive properties of the myocardium, and disruption of the mechanical linkage between the cytoskeleton and the cell membrane reduces the overall stiffness of the myocardium.

5.2 Methods

5.2.1 Mice

Two cardiac-specific Vcl knockout mouse lines provided by the lab of Robert Ross were used: a MLC2v-Cre/Vcl-Flox/Flox line where Vcl is reduced soon after birth (VclKO), and a Tamoxifen inducible line where knockout occurs in adulthood after tamoxifen has been administered to cause excision from the Vcl locus (TamoVclKO) [123]. Seven week-old male VclKO mice and WT littermates and 3-4 month-old male TamoVclKO mice (1 month after tamoxifen injections) were used for the papillary muscle experiments. All protocols were performed according to the National Institutes of Health's *Guide for the Care and Use of Laboratory Animals* and approved by the UCSD Animal Subjects Committee.

5.2.2 Papillary muscle isolation

The mice were first anesthetized with isoflurane and cervical dislocation was performed. The chest was opened and the heart arrested, dissected, cannulated and perfused with a modified Hepes buffered cardioplegic solution (137.2 mM NaCl, 15 mM KCl, 1.2 mM $MgCl_2$, 2.8 mM Na acetate, 10 mM taurine, 1 mM $CaCl_2$, 10 mM glucose, 10 mM Hepes, and 20 mM butanedione monoxime (BDM)) in equilibrium with 100% O_2. The right ventricle was opened and titanium oxide markers were placed on the papillary muscle (Figure 5.1). The papillary muscle was dissected and mounted in a tissue culture chamber filled with the cardioplegic solution [124].

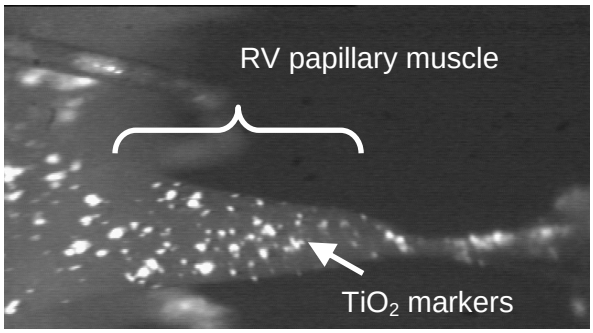

Figure 5.1: Digital recording of RV papillary muscle.

5.2.3 Papillary muscle stretching

The papillary muscle was attached to a stationary titanium hook and a force transducer attached to a micro-manipulated stage (Figure 5.2). During the mounting process, oxygen was also flowed over the top of the solution to prevent hypoxia. The cardioplegic solution was then exchanged for a Hepes buffered solution without BDM (137.2 mM NaCl, 5 mM KCl, 1.2 mM $MgCl_2$, 2.8 mM Na acetate, 10 mM taurine, 2 mM $CaCl_2$, 10 mM glucose, and 10 mM Hepes). The muscle was stimulated by the

titanium hook and a platinum electrode placed close to the base of the papillary muscle. After a one hour equilibration period, the muscle was paced at 1 Hz and stretched while the uniaxial force is recorded. Muscle lengths were acquired with a linear variable differential transformer, and a CCD camera recorded the local deformations of the muscle. Digital video recordings of muscle deformation were synchronized with the force data.

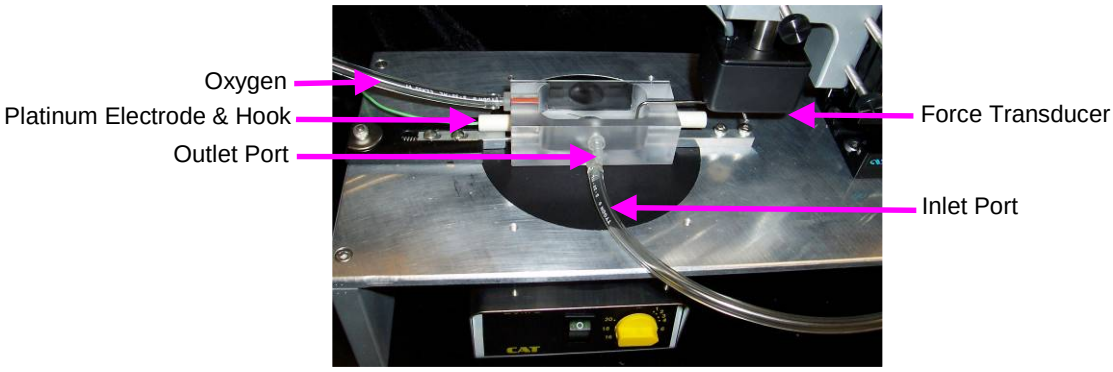

Figure 5.2: System for stretching mouse papillary muscles.

Stresses were calculated by dividing passive force data by the initial cross-sectional area of each muscle. Lagrangian uniaxial strain measurements were calculated with respect to the slack muscle. Exponentials were fit to the measured data to produce stress-strain curves.

5.2.4 MRI

Seven week-old VclKO (n = 3) and WT (n = 3) littermates were imaged prior to papillary muscle experiments. Global geometric and functional parameters such as EDV, ESV, SV, and EF were calculated as described in sections 2.3.3. - 2.3.5.

5.2.5 Tamoxifen injections

Three to four month-old TamoVclKOs were injected with tamoxifen (40 µg/g of body weight), a synthetic estrogen ligand, or corn oil (control) for 5 consecutive days (n = 2). One month after the start of injections, papillary muscles were excised and stretched.

5.2.6 Western blot analysis

Freshly isolated adult hearts were frozen in liquid nitrogen, pulverized and homogenized. Protein lysates were separated by sodium dodecyl sulfate-polyacrylamide gel electrophoresis and transferred to polyvinylidene difluoride membranes (Millipore, Bedford, MA). Membranes were blocked with PBS containing 0.1% Tween and 5% nonfat dry milk, and incubated with the primary antibodies overnight at 4°C. Blots were incubated overnight at 4°C with the primary antibodies: mouse monoclonal anti-pan-vinculin (detects vinculin and metavinculin), and anti-GAPDH. Bound antibodies were visualized by using secondary antibodies with horseradish peroxidase (Jackson ImmunoResearch Laboratories, West Grove, PA) and ECL reagents (Amersham Pharmacia Biosciences/GE Healthcare, Piscataway, NJ).

5.2.7 Statistics

All measurements are presented as mean ± SD. Global geometry and functional parameters were compared by Student's t test. Stress-strain curves were compared by two-way repeated measures ANOVA. P values < 0.05 were considered significant.

5.3 Results

5.3.1 MRI

Seven week-old VclKO and WT mice were imaged to determine global function (Figure 5.3). Calculations of ejection fractions (Table 5.1) indicated that there was no significant difference between 7 week old WT and VclKO mice. EDV was slightly higher in VclKOs compared to controls, but not significantly different.

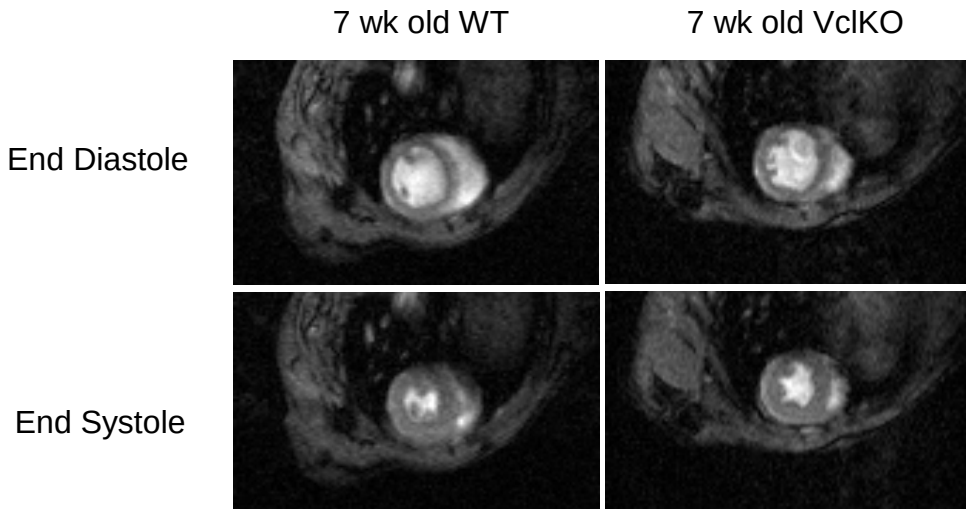

Figure 5.3: MR images of 7 week old WT and VclKO hearts.

Table 5.1: Global functional and geometric parameters of 7 week old VclKO and WT hearts

Mouse	EDV(ul)	ESV(ul)	EF(%)
WT	39 ± 2	15 ± 2	61 ± 4
VclKO	47 ± 7	21 ± 5	57 ± 5

5.3.2 Western blot

Four weeks after TamoVclKOs were injected with tamoxifen or corn oil (control), whole heart protein lysates were collected. Western blot analysis with GAPDH loading controls showed that hearts from mice injected with tamoxifen had a lower Vcl content than control hearts (Figure 5.4).

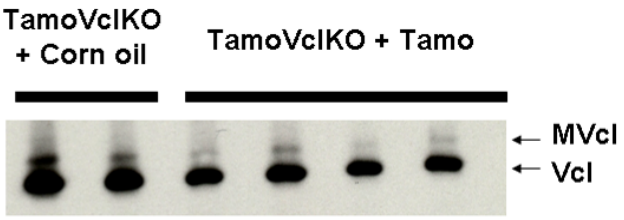

Figure 5.4: Vcl protein content is reduced in whole heart protein lysates of TamoVclKO mice 4 weeks after tamoxifen injections (courtesy of Amy Hsieh).

5.3.3 Stress strain curves

Papillary muscles from 7 week old VinKO mice and WT controls were stretched. Stress-strain curves were significantly different between WT and VclKO muscles (Figure 5.5). The slope of the WT curve was steeper than the VclKO curve at strains below 0.15. The slope of the VclKO curve was 20 - 60% less than in the WT curve. Thus, VclKO muscles were significantly more compliant in the fiber direction. Preliminary data (n = 2) from Tamo-VclKO mice suggest a similar trend. Mice injected with tamoxifen appear to have less stiff papillary muscles compared to mice injected with corn oil (Figure 5.6).

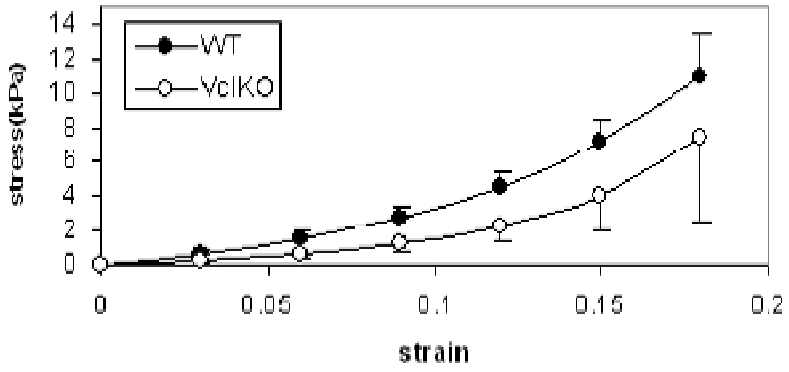

Figure 5.5: Stress strain curves of WT and VclKO muscles

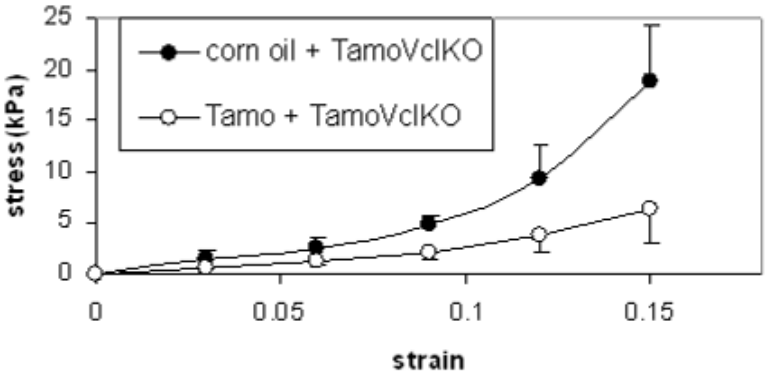

Figure 5.6: Stress strain curves of muscles from tamoxifen inducible mouse models.

5.4 Discussion

To study the effect of Vcl deletion on passive material properties of the myocardium, cardiac-specific Vcl knockout mouse lines were used. In the VclKO mouse model, Vcl is excised by Cre-LoxP technology (MLC2v-Cre recombinase promoter) in the neonatal heart. At 3 months of age, there is a 71% reduction of metavinculin (splice isoform of vinculin) which is specifically expressed in the cardiomyocyte. VclKO mice show progressive left ventricular dilation, abnormal

diastolic and systolic function, and high mortality, and DCM develops by 16 weeks of age [62]. It is important to study these mice before the onset of disease since there is a possibility that changes in the passive properties of the tissue are due to secondary effects besides Vcl deletion. For example, changes in the extracellular matrix commonly occur with heart failure. MRI was used to validate that the VclKO mice were not in failure. Ejection fraction was not significantly different in 7 week old VclKO and WT mice. VclKO hearts were slightly dilated, but not significantly larger than WT hearts. To test the mechanical properties of myocardial tissue, right ventricular papillary muscles were passively strained in the axial direction while simultaneously measuring force. Strain was measured through the use of surface markers. Sarcomere length is a major determinant of passive mechanics but was not available with the current experimental setup. However, it has been shown that surface marker displacements are proportional to sarcomere length changes as muscles are stretched [125]. The stress strain curves from 7 week old VclKOs indicated that the muscle was less stiff than WT tissue.

A TamoVclKO model was also used and Vcl was excised in a temporally controlled manner. TamoVclKOs were injected with tamoxifen such that Vcl knockdown was initiated in the adult heart rather than the neonatal heart. Therefore, Vcl was excised after the heart had a chance to fully develop. TamoVclKO mice eventually develop a dilated cardiomyopathic phenotype; however, echocardiography shows that there was no difference in fractional shortening one month after tamoxifen

injections. At this time point, preliminary data showed a more compliant stress-strain relationship in tamoxifen injected-mice compared to corn oil-injected mice.

Titin and ECM are major contributors to passive stiffness [126]. Histological evaluation of VclKO hearts at 12 weeks of age revealed mild fibrosis [62]. In this study, changes in ECM composition and structure were not quantified in the 7 week old hearts. Coiled perimysial collagen strands are orientated parallel to the cardiomyocytes in papillary muscles. As the muscle is stretched, the perimysial collagen coils straighten out and contribute to passive tension in the fiber direction [127]. Collagen content and structure will need to be quantified with picrosirius and trichrome staining [128,129] to ensure that ECM remodeling is not responsible for the observed changes in stiffness.

Studies in other mouse models have shown that deletion of structural proteins that stabilize linkages between the cytoskeleton and cell membrane, such as MLP [121], decreases passive stiffness in the myocardium. In this study, we showed that Vcl deletion leads to changes in passive stiffness prior to heart failure. Vcl deletion may disrupt the normal force transmission pathways from the ECM to cytoskeleton through the integrin-based costamere or cell-to-cell force transmission along the myocyte axis through the intercalated disc. These changes manifest as altered passive material properties of the myocardium. We conclude that Vcl contributes to the passive properties of the myocardium, and disruption of the mechanical linkage between the cytoskeleton and the cell membrane reduces the overall stiffness of the myocardium. Vcl also plays an important role in organizing the actin cytoskeleton. It has been found

that Vcl bundles cytoskeletal actin filaments into thicker, straight bundles [17]. Therefore, Vcl deletion may reduce the number of the thicker actin bundles, which may reduce the stiffness of the cardiomyocyte and papillary muscle. VclKO and TamoVclKO mice show altered passive material properties in the hearts before signs of heart failure. Therefore, the decrease in passive stiffness may be a primary cause of chamber dilatation, which ultimately leads to the development of DCM.

6 β1D integrin plays a role in anisotropic stretch-induced hypertrophy

6.1 Introduction

In healthy myocardium, the hypertrophic response is induced by increased load and biomechanical stress. There is a reactivation of embryonic genes for contractile proteins, ANF, and BNP. Protein synthesis and cardiomyocyte cell size also increase [37,130-132]. A common *in vivo* model of left ventricular hypertrophy uses aortic constriction to induce hemodynamic loading. For *in vitro* experiments, isolated neonatal rat ventricular cardiomyocytes (NRVM) are plated on elastic membranes and stretched uniaxially by 10 to 20% to induce hypertrophy [133-136]. A multiaxial stretcher has also been developed which produces anisotropic stretch in a more physiological manner [137]. Neonatal cardiomyocytes were aligned using micropatterning techniques and took on a rod like shape, similar to the *in vivo* adult

cardiomyocyte. It was shown that in aligned cultures of NRVM, predominantly transverse stretch induced greater hypertrophic signals compared to axial or longitudinal stretch [137,138]. ANF, Connexin-43, and N-cadherin levels were increased with transverse stretch compared to longitudinal stretch. Pulse-chase experiments have also demonstrated that contractile protein turnover is suppressed by uniaxial stretch transverse to the myofiber axis, thus, promoting the accumulation of myofibril units. However, when cardiomyocytes are stretched longitudinally, there is no effect on contractile protein turnover [139]. FAK and ERK1/2 phosphorylation are also increased to higher levels with transverse stretch than longitudinal stretch [140].

Cardiomyocytes respond to mechanical load through the mechanisms of mechanotransduction, where forces acting mechanosensors are transduced into a cascade of biochemical signals that induce the hypertrophic response [141,142]. Different transmembrane mechanosenors have been identified. When the plasma membrane is deformed, the pore size of stretch activated channels changes and alters the intracellular concentration of ions such as Ca^{2+}. Cell surface receptors (G-protein coupled receptors and growth factor receptors) have been shown to be activated by mechanical stretch in the absence of agonist ligands [143]. Cell-matrix interactions have been previously implicated in mechanotransduction. In the costamere, integrins are transmembrane proteins that are positioned to transduce physical forces at the plasma membrane into cytoplasmic chemical signals. Integrin mediated hypertrophic signaling has been associated with several early signaling molecules. Focal adhesion kinase (FAK) is activated in cardiomyocytes exposed to cyclic stretch and in pressure

overloaded myocardium [38]. Inhibition of FAK phosphorylation also leads to lower ANF expression. FAK can bind to β1 integrin tails [39]. Upon integrin binding, autophosphorylation of Tyr-397 occurs, thus, creating a strong binding site for c-Src [40]. The Fak/Src complex can lead to activation of ERK1/2 [41]. FAK has also been shown to activate p38MAPK during stretch induced hypertrophy [42] as well as the JNK pathway [43].

Due to its location in the costamere and known association with cytoplasmic signaling molecules, β1D integrin may play a role in the directional sensitivity of mechanotransduction. In this study, NRVM were aligned and stretched predominantly in the transverse or longitudinal direction. β1D integrin function was disrupted by overexpression of a dominant negative chimeric protein which expresses the cytoplasmic domain of β1D integrin. We hypothesized that β1D integrin disruption would abolish the directional sensitivity to stretch such that transverse stretch would induce levels of ANF similar to those produced by longitudinal stretch. With real time-quantitative PCR, it was determined that β1D integrin disruption blunted the difference in ANF expression between transversely and axially stretched cells.

6.2 Methods

6.2.1 Cell isolation

Two day-old NRVM were isolated and cultured using the Neomyts Cardiomyocyte Isolation Kit (Cellutron, Highland Park, NJ) following the manufacturer's instructions. All protocols were performed according to the National

Institutes of Health's *Guide for the Care and Use of Laboratory Animals* and approved by the UCSD Animal Subjects Committee.

6.2.2 Cell alignment

Soft lithography techniques [144] were used to create silicone membranes with 10 um wide channels that are 5 um deep. A silicon wafer was spin-coated with negative photoresist, SU-8 5 (Micro-chem, Inc., Santa Clara, CA), to create a 5 um-thick film. The wafer was then baked on a hot plate at 65 °C for two minutes and then at 9 °C for an additional five minutes. The resist was then exposed to UV light via mask aligner (Quintel, Morgan Hill, CA) using a chrome-on-quartz photomask (Advanced Reproduction, North Andover, MA). The wafer was then baked again at 65 °C for two minutes and then at 95 °C for two minutes, and then developed in SU-8 developer (Microchem,Inc.) for 3 min and rinsed with isopropyl alcohol.

The micropatterned wafer was used to cast silicone membranes. Polydimethylsiloxane (PDMS) solution was mixed using the Sylgard 186 Silicone Elastomer Kit (Dow Corning, Midland, MI). PDMS was degassed and spun onto the micropatterned wafers at 650 RPM for 30 seconds. The PDMS was baked for 2 hours at 65°C and peeled off the mold. The PDMS membranes were cleaned with 70% ethanol and PBS rinses.

6.2.3 Anisotropic cell stretching

The anisotropic cell stretcher has a 2:1 ellipticity. Thus, the ratio of maximum-to-minimum principal stretch is 2:1. The maximum principal stretch is along the minor axis of the ellipse (Figure 6.1).

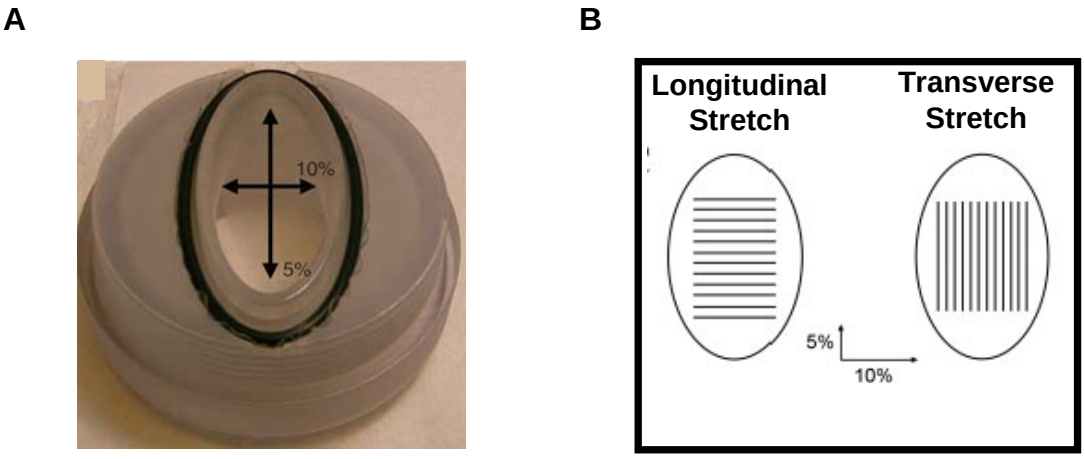

Figure 6.1: Elliptical cell stretcher (A) produces anisotropic stretch (B).

Micropatterned silicone membranes were attached to the stretchers and cells were oriented parallel or perpendicular to the minor axis of the ellipse for longitudinal or transverse stretching respectively (Figure 6.1B). The membranes were coated with laminin. Three million neonatal rat ventricular cardiomyocytes were plated on each laminin coated membrane (Figure 6.2).

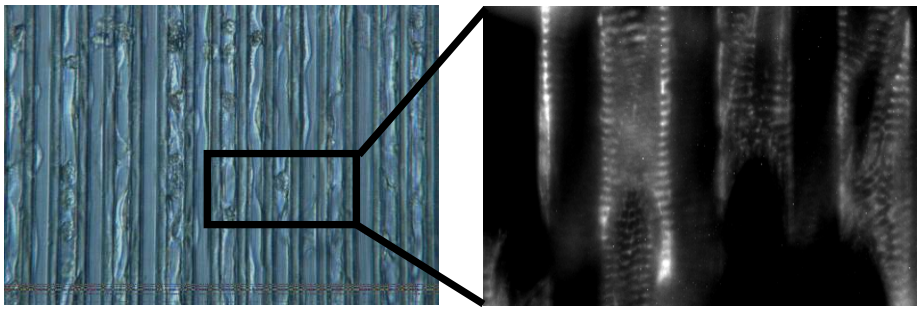

Figure 6.2: Sarcomeric alpha-actinin staining of cardiomyocytes plated in micropatterned channels shows highly organized and aligned sarcomeres

Cells were allowed to attach overnight in plating media (80% DMEM and 20% M199 supplemented with 10% horse serum, 5% fetal bovine serum, and 1% penicillin/

streptomycin). The next day the plating media was exchanged for maintenance media (80% DMEM and 20% M199 with 1% fetal bovine serum). The following day, cells were infected with adenovirus. Eight hours later, cells were statically stretched for 24 hours at 10%/5% stretch.

6.2.4 Virus

Tac β1D adenovirus was used to disrupt native integrin function (Figure 6.3). Tac β1D contains the extracellular and transmembrane Tac subunit of the interleukin-2 receptor and the cytoplasmic domain of β1D integrin. Tac β1D overexpression has a dominant negative effect on native integrins. Tac α5 contains the cytoplasmic domain of α5 integrin. Overexpression of Tac α5 lacks the inhibitory effect of Tac β1D and is used as a control virus [145]. Plaque assays were performed to measure the titer of the adenovirus stocks.

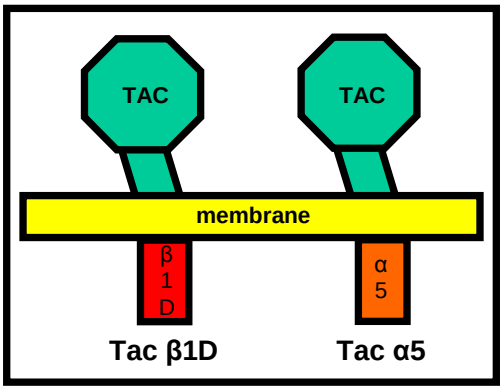

Figure 6.3: Tac β1D and Tac α5 proteins.

6.2.5 Cell adhesion assay

Cardiomyocytes were aligned on micropatterned membrane and infected with Tac α5 and Tac β1D virus at different multiplicity of infections (MOIs). After 32 hours,

unattached cells were removed by gentle shaking. Cells were fixed with 4% paraformaldehyde (PFA) and stained with 5 mg/ml Crystal Violet in 20% methanol overnight. The stained cells were solubilized with 2% SDS and absorbance was measured at 590 nm.

6.2.6 Real time quantitative PCR (RT-qPCR)

After 24 hours of stretch, cells were lysed and RNA was isolated. RNA was extracted with Qiagen's RNeasy Micro RNA purification kit. DNase treatment was used to remove genomic DNA. A Nanodrop spectrophotometer was used to measure the RNA concentration. Reverse transcription was accomplished using Applied Biosystem's High capacity cDNA reverse Transcription kit. RT-qPCR was performed using Applied Biosystem's 7700 real time thermal cycler, Taqman Universal Master Mix, and pre-made primers and Taqman probes for ANF and glyceraldehyde 3-phosphate dehydrogenase (GAPDH). GAPDH is a housekeeper gene and was used as an internal control. For each RNA sample, triplicate cycle threshold (Ct) values were measured and averaged. The ΔΔCt method was used to quantify the relative changes in ANF gene expression.

6.2.7 Staining

Cells were fixed with 4% PFA, permeabilized in 0.2% Triton X-100/PBS, and blocked with 3% BSA and 3% goat serum in PBS. Primary antibodies for vinculin and α-actinin were applied overnight at 4°C. Also, a mouse monoclonal antibody 7G7/B6 (American Type Culture Collection, Manassas, VA) was used to detect the interleukin-2

receptor extracellular Tac domain. After washing, Alexa-488 secondary antibody was applied for 30 min at room temperature.

6.2.8 Statistics

All measurements are presented as mean ± SD. RT-qPCR results were analyzed by two-way ANOVA. P values < 0.05 were considered significant.

6.3 Results

6.3.1 Cell adhesion assay

Results from the cell adhesion assay showed that cardiomyocytes infected with Tac β1D had lower cell adhesion than cells infected with Tac α5 at 5 MOI (Figure 6.4). To achieve the highest level of Tac β1D expression without affecting cell adhesion, cardiomyocytes were infected with adenovirus at 3 MOI for stretch experiments.

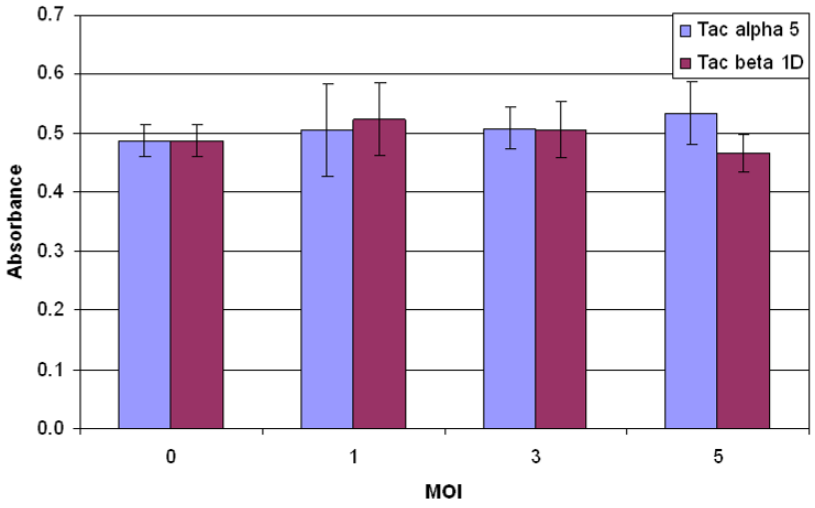

Figure 6.4: Cell adhesion assay results show that cell adhesion starts to decrease at 5 MOI of Tac β1D.

6.3.2 Staining

Figure 6.5 shows staining of sarcomeric and costameric proteins in cardiomyocytes plated on laminin coated micropatterned membranes. In the micropatterned membranes, the cardiomyocytes appear elongated in the channels. Sarcomeric α-actinin staining showed sarcomere alignment with the long-axis of the cell. Vinculin was also expressed in a periodic pattern along the cell membrane. Cells infected with Tac β1D and Tac α5 adenovirus (3 MOI) for 32 hours were stained with anti-Tac antibody. Figure 6.6 shows that Tac β1D and Tac α5 were readily expressed in cardiomyocytes after 32 hours of infection.

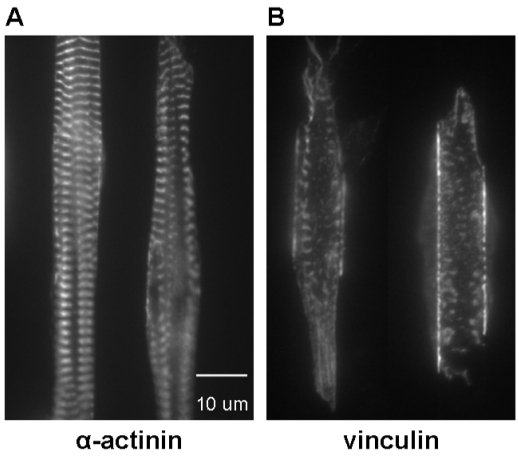

Figure 6.5: Staining of sarcomeric α-actinin (A) and vinculin (B) in aligned cardiomyocytes.

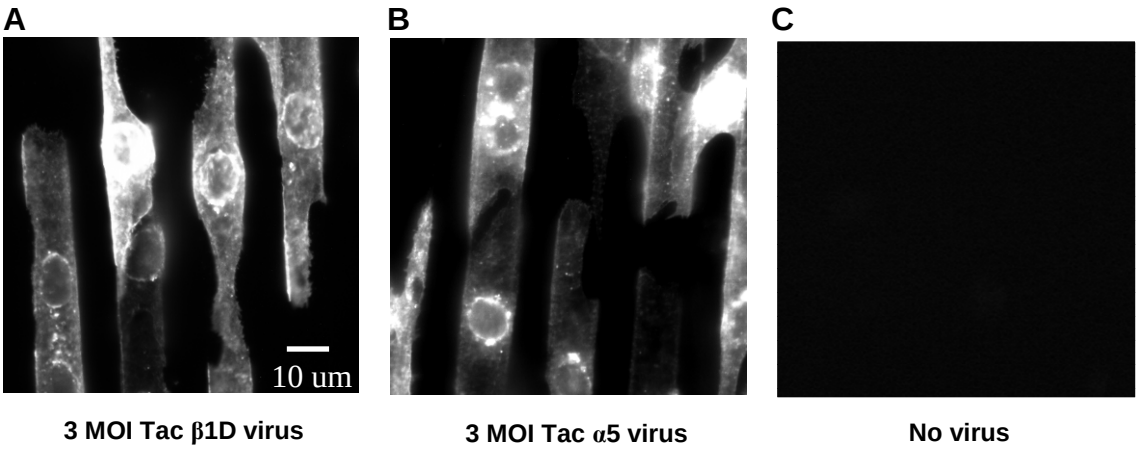

Figure 6.6: Anti-Tac antibody staining in aligned cardiomyocytes infected with Tac β1D adenovirus (A), Tac α5 adenovirus (B), and no virus (C).

6.3.3 RT-qPCR

ANF expression levels were normalized to unstretched levels (Figure 6.7). As expected, ANF levels in control (Tac α5 infected) cells were significantly higher ($P < 0.05$**) with transverse stretch than with longitudinal stretch. With transverse stretch, ANF expression in Tac β1D infected cells was significantly lower ($P < 0.05$*) compared to Tac α5 infected cells. There was no significant difference in ANF levels between longitudinally stretched Tac α5 and Tac β1D infected cells.

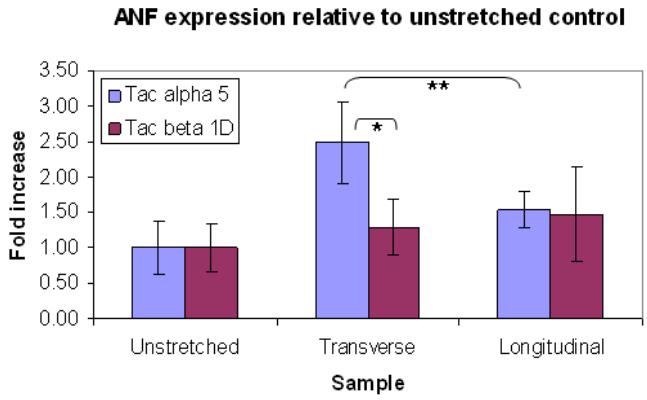

Figure 6.7: With transverse stretch, Tac β1D infected cells express relatively less ANF compared to Tac α5 infected cells ($P < 0.05$*).

6.4 Discussion

To study the role of β1D integrin in anisotropic stretch-induced hypertrophy, the cardiomyocytes needed to be cultured in an aligned pattern. Micropatterning techniques have been previously used to orient cells in one direction [146-148]. In this study, cardiomyocytes were cultured in 10 μm wide channels with a 5 μm depth. Previously published studies have shown that this particular channel geometry leads to highly oriented cardiomyocytes with elongated rod-like shapes [148]. Antibody labeling of α-actinin also showed a highly organized sarcomeric pattern. Staining of vinculin revealed costameric structures at the membrane with the same periodicity as the z-disc staining. Thus, the *in vitro* culture system is able to capture many characteristics found with the *in* vivo cardiomyocyte morphology. Laminin was chosen as the extracellular matrix protein since it is the main binding partner of the α7β1 integrin heterodimer in cardiac tissue [149].

β1D integrin function was disrupted with the use of the Tac β1D adenovirus. Tac β1D is a dominant negative inhibitor of native β1 integrins and competes for cytoplasmic binding partners needed for signaling. In post-natal cardiomyocytes, the predominant β1 isoform is β1D; therefore, it is assumed that the changes seen are a result of β1D integrin inhibition. The use of Tac chimera proteins for integrin inhibition has been previously published [150-154]. Overexpression of β1 integrin cytoplasmic domains has been shown to inhibit adrenergic induction of ANF in NRVMs with phenylephrine [152]. Disruption of β1 signaling with Tac β1D also significantly inhibited stretch-dependent activation of ERK, p38, and JNK [153]. Most signaling

molecules interact with the β subunit of the integrin heterodimer and not the α subunit. Therefore, Tac α5 lacks the dominant negative inhibitory activity of Tac β1D and can be used as a control virus [154].

In mechanical signaling studies, it is important to control for cell adhesion. The cell phenotype and force transmitted from extracellular matrix to the cell are dependent on cell adhesion [155]. At high concentrations, Tac β1D virus causes cells to detach from the ECM substrate. The cell adhesion assay allowed us to choose the highest level of Tac β1D infection without affecting cell adhesion. Although the chosen infection level of 3 MOI was considerably low, anti-Tac staining showed expression of the Tac chimera protein in infected cells. By controlling for cell adhesion, the resulting changes in ANF expression are more likely the result of integrin function inhibition and not from decreased cell adhesion.

For control (Tac α5 integrin infected) cells, ANF expression levels in transversely stretched cells were significantly higher than in longitudinally stretched cells, which corresponded with previous western blot data of ANF protein [137]. However, when integrin function was disrupted with Tac β1D overexpression, the difference in ANF levels between transversely and longitudinally stretched cells was blunted. In fact, there was no significant difference between the two groups. The levels of transverse stretch-induced ANF were affected more by Tac β1D overexpression than longitudinally stretched cells. With transverse stretch, Tac β1D infected cells expressed significantly less ANF than Tac α5 infected cells. However, no difference was seen with longitudinal stretch. These results suggest that β1D integrin,

the dominant β integrin in post-natal cardiomyocytes, plays a role in anisotropic stretch-induced hypertrophy and may be particularly important for mechanotransduction of transverse stretch. For Tac β1D infected cells, ANF levels were relatively unchanged with longitudinal stretch, which may be due to the existence of other mechanosenors that are not dependent on β1D integrin. These mechanosensors are still able to sense the longitudinal stretch and activate the appropriate signaling pathways.

The location of β1D integrin circumferentially around the cell (transverse to the long axis) may be responsible for the cardiomyocyte's directional sensitivity to transverse stretch. Specific directions and magnitudes of stretch regulate mechanotransduction in cardiomyocytes; therefore, different signaling cascades might be associated with longitudinal versus transverse stretch. ANF is a fairly downstream marker of hypertrophic signaling. It would be interesting to examine earlier signaling molecules. There may be differential activation of FAK, ERK, ILK, p38MAPK, Akt, or JNK, which have been linked to the integrin-based costamere [156]. Induction of immediate-early genes such as c-fos, c-jun, c-myc, JE, and Egr-1 may also be affected [134].

7 Summary and Conclusions

7.1 Effect of vinculin deletion on LV mechanics

To study the effects of Vcl deletion on LV global and regional mechanics, the VclKO mouse model was used where cardiomyocytes were specifically made deficient in Vcl. In VclKO hearts, the LVs were enlarged and ejection fraction was lower compared to WT hearts. 3D strain analysis revealed differences in LV wall mechanics between WT and VclKO mice at 8 weeks of age when systolic function had declined. Most notably, end-systolic radial strain and torsional shear were reduced in VclKO hearts which contributed to a decreased ejection fraction. These changes in geometry and function are consistent with human cases of dilated cardiomyopathy. Thus, this mouse model is able to reproduce many of the clinical features of human dilated cardiomyopathy and heart failure.

To determine if Vcl played a role in fiber/sheet mechanics prior to the onset of heart failure, fiber and sheet orientations were obtained from histological measurements

to calculate 3D strains in the fiber and sheet coordinates. In VclKO mice, it was found that there was a decrease in the magnitude of end-systolic sheet extension and interlaminar shear compared to WT mice; however, fiber strains remained unchanged. The decrease in sheet extension may be due to an increase in stiffness in the sheet direction. The reduction in sheet strain results in decreased wall thickening, which leads to a decrease in interlaminar shear.

7.2 Effect of vinculin deletion on passive material properties

We hypothesized that deletion of the costameric protein Vcl would lead to changes in passive stiffness prior to the onset of systolic dysfunction. Vcl deletion may disrupt the normal force transmission pathways from ECM to cytoskeleton through the integrin-based costamere or cell-to-cell force transmission along the myocyte axis, which may manifest as altered passive material properties of the myocardium.

To test the mechanical properties of myocardial tissue, murine right ventricular papillary muscles were passively strained in the axial direction while simultaneously measuring force. Papillary muscles from 7 week old VclKO mice and WT controls were isolated and stretched. Stress-strain analysis was used to measure passive stiffness in the direction of myocardial fibers.

Stress-strain curves were significantly different between WT and VclKO papillary muscles ($P<0.05$). The slope of the VinKO curve was less than in the WT curve, indicating that VclKO muscles are more compliant in the fiber direction. The data suggests that Vcl contributes to the passive mechanical properties of the myocardium. Weakening of the mechanical linkage between the cytoskeleton and the

cell membrane and reorganization of the cytoskeleton may reduce the overall stiffness of the cardiomyocyte.

7.3 Model of VclKO myocardium

A simple model of the VclKO myocardium based on the results of the papillary muscle stretching data (Chapter 5) and the *in vivo* 3D strain analysis (Chapter 4) can be created. Stress-strain curves of RV papillary muscles indicated that VclKO tissue is more compliant in the fiber direction than WT tissue. The *in vivo* 3D strain analysis showed that there was decreased systolic sheet extension in VclKOs, which implies that the myocardium is stiffer in the sheet direction. However, fiber shortening was unaffected by Vcl deletion.

In the model of the VclKO myocardium (Figure 7.1), the overall stiffness of the cardiomyocytes has decreased. The cells are softer due to destabilization of the integrin-cytoskeletal linkage and possible reorganization of the actin cytoskeleton. The decrease in passive stiffness does not interfere with the cell's ability to contract since fiber shortening is unaffected. In the laminar sheet, adjacent cells are coupled by an increased number of endomysial collagen struts in the transverse direction. The sheets are surrounded by an isotropic network of perimysial collagen strands. The components of this model allow the VclKO tissue to be stiffer in the sheet direction and less stiff in the fiber direction. To determine if this model is accurate, scanning electron microscopy can be used to evaluate the number of endomysial collagen struts between adjacent cells. Computational modeling may also help determine if the proposed material properties lead to the observed systolic strains.

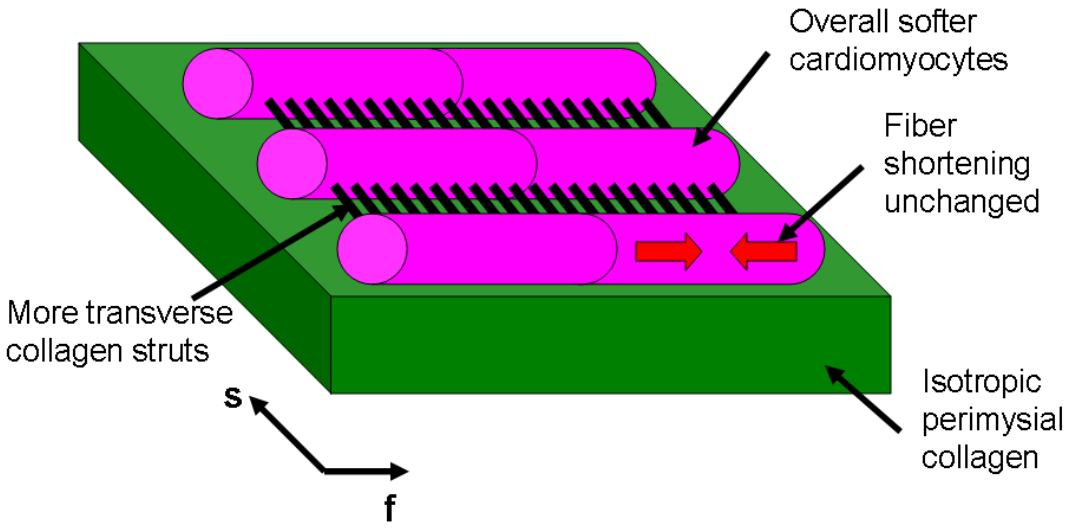

Figure 7.1: A model of the VclKO myocardium is stiffer in the sheet direction and less stiff in the fiber direction.

7.4 Effects of β1D integrin disruption on anisotropic hypertrophy

In healthy myocardium, cardiomyocytes hypertrophy in response to increased load. With development of this growth response, expression of ANF rises. In cultured cardiomyocytes, previous work has shown that transverse stretch increased hypertrophic signals more than longitudinal stretch. Due to its location in the costamere and known association with cytoplasmic signaling molecules, we hypothesized that integrins would play an important role in the directional sensitivity of mechanotransduction in cardiomyocytes.

Neonatal rat ventricular myocytes were cultured in an aligned pattern on anisotropic stretching devices. The cells were then infected with an adenovirus to

disrupt native integrin function (Tac β1D) or a control virus (Tac α5), and stretched predominantly along their longitudinal or transverse axes for 24 hours. Real time quantitative PCR was performed to analyze changes in ANF gene expression. ANF expression levels in the stretched cells were normalized to unstretched cells.

Control (Tac α5 integrin infected) cells displayed ANF expression in transversely stretched cells that was significantly higher than in longitudinally stretched cells. However, when integrin function was disrupted with Tac β1D overexpression, the difference in ANF levels between transversely and longitudinally stretched cells was blunted. ANF levels in cells stretched in the transverse direction were affected the most. These results suggest that β1D integrin, the dominant β integrin in post-natal cardiac myocytes, plays a role in anisotropic stretch-induced hypertrophy. The location of β1D integrin in the costamere, which is located circumferentially around the cell, may be responsible for the cardiomyocyte's directional sensitivity to transverse mechanical stimuli.

7.5 Future directions

7.5.1 Material properties

Since costameres are oriented circumferentially around the cardiomyocyte and perpendicular to the long axis of the cell, they help transmit force laterally across the cardiomyocytes to the ECM. Thus, passive material properties in the cross-fiber direction of the myocardium may be altered by costameric disruption. With the papillary muscle stretching experiments (Chapter 5), only passive material properties in the fiber direction were measured. Material properties in the cross-fiber direction could

not be studied with this particular experimental setup. It is likely that force transmission in the cross-fiber direction of the myocardium is altered by costameric disruption. In the diaphragm muscle, it has been shown that integrin deletion in striated muscle leads to a lower stiffness in the cross fiber direction [149]. With *in vivo* MRI and LV pressure measurements, we can use computational modeling to determine material properties in the cross-fiber direction in Vcl or β1D integrin KO hearts.

In order to study anisotropic material properties, Millar catheterization can be performed after *in vivo* imaging (Chapter 3) to obtain accurate pressure information [78]. After Millar catheterization, the heart is excised from the mouse and fixed. Diffusion tensor MRI can then be used to gain information on the fiber and sheet structures throughout the entire heart [115]. To estimate material properties, a 3D model of the LV is created. Using early diastolic images from cine MRI, the 3D geometry of the LV can be reconstructed as described in Chapter 2. Fiber angles from the DTMRI data are input into the geometric model. The finite element model is loaded with early to late LV diastolic pressures. Material constants of the strain energy function are optimized iteratively such that the weighted difference between the model and experimental pressure-strain relationship is minimized, and sheet stiffness can be calculated [157].

7.5.2 β1 splice variant specific signaling

There are several isoforms of β1 integrin which are produced through splicing of a distinct exon within the β1 gene which produces a unique C-terminal portion of the β1 cytoplasmic tail. β1D integrin is exclusively expressed in striated muscle and is the

main β1 integrin isoform expressed in the post natal heart. β1A integrin is another splice variant isoform of β1 integrin which is normally expressed in the embryonic heart. β1A integrin may function similarly to β1D integrin in mechanotransduction. However, some data suggests that β1D integrin may have unique properties that may impact mechanotransduction. For example, β1D integrin binds more tightly to talin than β1A integrin and forms more stable cytoskeletal-ECM connections [158]. This may lead to stronger stretch induced signaling through β1D integrin as opposed to β1A. To study the roles of the different β1 splice variants, one can attempt to rescue function in β1 integrin deficient cells by overexpression of β1A integrin or β1D integrin.

Neonatal ventricular myocytes deficient in β1 integrin can be derived from the Tamo-β1KO mice. Pregnant Tamo-β1KO mice are injected with tamoxifen during pregnancy. Neonatal cardiomyocytes isolated from pups are plated on patterned membranes as described in Chapter 6. However, during plating, the cells are infected with recombinant adenoviruses expressing β1A integrin or β1D integrin. Two days after viral infection, the cells can be stretched and analyzed for ANF expression and other signaling molecules induced by stretch.

7.6 Conclusions

Deletion or disruption of critical costameric proteins leads to alterations in ventricular mechanics, passive material properties, and hypertrophic signaling. All of these changes can contribute to the development of dilated cardiomyopathy and eventually heart failure. A decrease in passive stiffness, as seen in VclKO papillary muscle, may be one of the initiating factors that cause ventricular dilation. Extensive

dilation may negatively impact the performance of the heart. A decrease in interlaminar shear as well sheet extension reduces systolic wall thickening and leads to insufficient stroke volume. The combination of these factors, which all result from changes in force transmission, may cause dilation and insufficient pumping action which are characteristic of dilated cardiomyopathy.

In addition to causing cardiac dysfunction through altered force transmission, defects in the costamere can also alter mechanotransduction pathways. Cardiomyocytes are able to distinguish between different directions of stretch and different signaling pathways are activated depending on the loading pattern. Disruption of β1D seems to abolish the cardiomyocyte's sensitivity to transverse stretch. Defects in the normal mechanotransduction pathways do not allow the heart to respond properly to mechanical stimuli. Thus, the myocardium is unable to hypertrophy and compensate for an increase in wall stress. An inadequate level of hypertrophic remodeling may ultimately lead to cardiac dysfunction and failure.

References

1. Gregorio CC, Antin PB. To the heart of myofibril assembly. Trends in Cell Biology, 2000;10:355-362.

2. Ervasti J. Costameres: the Achilles' Heel of Herculean Muscle. J Biol Chem 2003;278:13591-13594.

3. Heart Failure. http://www.americanheart.org. 12/25/2009.

4. Luk A, Ahn E, Soor GS, Butany J. Dilated cardiomyopathy: a review. Journal of Clinical Pathology 2009;62:219-225.

5. Ku L, Feiger J, Taylor M, Mestroni L, on behalf of the Familial Cardiomyopathy Registry,. Familial Dilated Cardiomyopathy. Circulation 2003;108:e118-121.

6. Arber S, Hunter JJ, Ross J, Hongo M, Sansig G, Borg J, Perriard J, Chien KR, Caroni P. MLP-Deficient Mice Exhibit a Disruption of Cardiac Cytoarchitectural Organization, Dilated Cardiomyopathy, and Heart Failure. Cell 1997;88:393-403.

7. Arimura T, Hayashi T, Terada H, Lee S, Zhou Q, Takahashi M, Ueda K, Nouchi T, Hohda S, Shibutani M, Hirose M, Chen J, Park J, Yasunami M, Hayashi H, Kimura A. A Cypher/ZASP Mutation Associated with Dilated Cardiomyopathy Alters the Binding Affinity to Protein Kinase C. Journal of Biological Chemistry 2004;279:6746-6752.

8. Pashmforoush M, Pomies P, Peterson KL, Kubalak S, Ross J, Hefti A, Aebi U, Beckerle MC, Chien KR. Adult mice deficient in actinin-associated LIM-domain protein reveal a developmental pathway for right ventricular cardiomyopathy. Nat Med 2001;7:591-597.

9. Kaplan SR, Gard JJ, Protonotarios N, Tsatsopoulou A, Spiliopoulou C, Anastasakis A, Squarcioni CP, McKenna WJ, Thiene G, Basso C, Brousse N, Fontaine G, Saffitz JE. Remodeling of myocyte gap junctions in arrhythmogenic right ventricular cardiomyopathy due to a deletion in plakoglobin (Naxos disease). Heart Rhythm 2004;1:3-11.

10. Rampazzo A, Nava A, Malacrida S, Beffagna G, Bauce B, Rossi V, Zimbello R, Simionati B, Basso C, Thiene G, Towbin JA, Danieli GA. Mutation in Human Desmoplakin Domain Binding to Plakoglobin Causes a Dominant Form of Arrhythmogenic Right Ventricular Cardiomyopathy. The American Journal of Human Genetics 2002;71:1200-1206.

11. Fatkin D, MacRae C, Sasaki T, Wolff MR, Porcu M, Frenneaux M, Atherton J, Vidaillet HJ,Jr, Spudich S, De Girolami U, Seidman JG, Seidman C, Muntoni F, Muehle G, Johnson W, McDonough B. Missense mutations in the rod domain of the lamin A/C gene as causes of dilated cardiomyopathy and conduction-system disease. N Engl J Med 1999;341:1715-1724.

12. Brodsky GL, Muntoni F, Miocic S, Sinagra G, Sewry C, Mestroni L. Lamin A/C gene mutation associated with dilated cardiomyopathy with variable skeletal muscle involvement. Circulation 2000;101:473-476.

13. Li D, Tapscoft T, Gonzalez O, Burch PE, Quinones MA, Zoghbi WA, Hill R, Bachinski LL, Mann DL, Roberts R. Desmin mutation responsible for idiopathic dilated cardiomyopathy. Circulation 1999;100:461-464.

14. Muntoni F, Torelli S, Ferlini A. Dystrophin and mutations: one gene, several proteins, multiple phenotypes. The Lancet Neurology 2003;2:731-740.

15. Karkkainen S, Miettinen R, Tuomainen P, Karkkainen P, Helio T, Reissell E, Kaartinen M, Toivonen L, Nieminen MS, Kuusisto J, Laakso M, Peuhkurinen K. A novel mutation, Arg71Thr, in the delta-sarcoglycan gene is associated with dilated cardiomyopathy. J Mol Med 2003;81:795-800.

16. Tsubata S, Bowles KR, Vatta M, Zintz C, Titus J, Muhonen L, Bowles NE, Towbin JA. Mutations in the human delta-sarcoglycan gene in familial and sporadic dilated cardiomyopathy. J Clin Invest 2000;106:655-662.

17. Olson T, Illenberger S, Kishimoto N, Huttelmaier S, Keating M, Jockusch B. Metavinculin Mutations Alter Actin Interaction in Dilated Cardiomyopathy. Circulation 2002;105:431-437.

18. Tardiff JC. Sarcomeric proteins and familial hypertrophic cardiomyopathy: linking mutations in structural proteins to complex cardiovascular phenotypes. Heart Fail Rev 2005;10:237-248.

19. Olson TM, Michels VV, Thibodeau SN, Tai YS, Keating MT. Actin mutations in dilated cardiomyopathy, a heritable form of heart failure. Science 1998;280:750-752.

20. Kamisago M, Sharma SD, DePalma SR, Solomon S, Sharma P, McDonough B, Smoot L, Mullen MP, Woolf PK, Wigle ED, Seidman JG, Seidman CE. Mutations in sarcomere protein genes as a cause of dilated cardiomyopathy. N Engl J Med 2000;343:1688-1696.

21. Olson TM, Kishimoto NY, Whitby FG, Michels VV. Mutations that alter the surface charge of alpha-tropomyosin are associated with dilated cardiomyopathy. J Mol Cell Cardiol 2001;33:723-732.

22. Squire JM. Architecture and function in the muscle sarcomere. Current Opinion in Structural Biology, 1997;7:247-257.

23. Granzier H, Labeit S. Cardiac titin: an adjustable multi-functional spring. J Physiol 2002;541:335-342.

24. Clark KA, McElhinny AS, Beckerle MC, Gregorio CC. STRIATED MUSCLE CYTOARCHITECTURE: An Intricate Web of Form and Function . Annual Review of Cell and Developmental Biology 2002;18:637-706.

25. Perriard J, Hirschy A, Ehler E. Dilated Cardiomyopathy: A Disease of the Intercalated Disc? Trends in Cardiovascular Medicine, 2003;13:30-38.

26. Ross R, Borg T. Integrins and the Myocardium. Circ Res 2001;88:1112-1119.

27. Sharp WW, Simpson DG, Borg TK, Samarel AM, Terracio L. Mechanical forces regulate focal adhesion and costamere assembly in cardiac myocytes. Am J Physiol Heart Circ Physiol 1997;273:H546-556.

28. Danowski B, Imanaka-Yoshida K, Sanger J, Sanger J. Costameres are sites of force transmission to the substratum in adult rat cardiomyocytes. J Cell Biol 1992;118:1411-1420.

29. Mansour H, de Tombe PP, Samarel AM, Russell B. Restoration of Resting Sarcomere Length After Uniaxial Static Strain Is Regulated by Protein Kinase C{epsilon} and Focal Adhesion Kinase. Circ Res 2004;94:642-649.

30. Bovendeerd PH, Arts T, Huyghe JM, van Campen DH, Reneman RS. Dependence of local left ventricular wall mechanics on myocardial fiber orientation: a model study. J Biomech 1992;25:1129-1140.

31. LeGrice IJ, Smaill BH, Chai LZ, Edgar SG, Gavin JB, Hunter PJ. Laminar structure of the heart: ventricular myocyte arrangement and connective tissue architecture in the dog. Am J Physiol Heart Circ Physiol 1995;269:H571-582.

32. Legrice IJ, Hunter PJ, Smaill BH. Laminar structure of the heart: a mathematical model. Am J Physiol Heart Circ Physiol 1997;272:H2466-2476.

33. Costa KD, Takayama Y, McCulloch AD, Covell JW. Laminar fiber architecture and three-dimensional systolic mechanics in canine ventricular myocardium. Am J Physiol Heart Circ Physiol 1999;276:H595-607.

34. LeGrice IJ, Takayama Y, Covell JW. Transverse Shear Along Myocardial Cleavage Planes Provides a Mechanism for Normal Systolic Wall Thickening. Circ Res 1995;77:182-193.

35. Ashikaga H, Covell JW, Omens JH. Diastolic dysfunction in volume-overload hypertrophy is associated with abnormal shearing of myolaminar sheets. Am J Physiol Heart Circ Physiol 2005;288:H2603-H2610.

36. Ashikaga H, Criscione JC, Omens JH, Covell JW, Ingels NB, Jr. Transmural left ventricular mechanics underlying torsional recoil during relaxation. Am J Physiol Heart Circ Physiol 2004;286:H640-647.

37. Frey N, Olson EN. CARDIAC HYPERTROPHY: The Good, the Bad, and the Ugly. Annual Review of Physiology 2003;65:45-79.

38. Franchini KG, Torsoni AS, Soares PHA, Saad MJA. Early Activation of the Multicomponent Signaling Complex Associated With Focal Adhesion Kinase Induced by Pressure Overload in the Rat Heart. Circ Res 2000;87:558-565.

39. Liu S, Calderwood D, Ginsberg M. Integrin cytoplasmic domain-binding proteins. J Cell Sci 2000;113:3563-3571.

40. Calalb M, Polte T, Hanks S. Tyrosine phosphorylation of focal adhesion kinase at sites in the catalytic domain regulates kinase activity: a role for Src family kinases. Mol Cell Biol 1995;15:954-963.

41. Domingos PP, Fonseca PM, Nadruz W, Jr., Franchini KG. Load-induced focal adhesion kinase activation in the myocardium: role of stretch and contractile activity. Am J Physiol Heart Circ Physiol 2002;282:H556-564.

42. Aikawa R, Nagai T, Kudoh S, Zou Y, Tanaka M, Tamura M, Akazawa H, Takano H, Nagai R, Komuro I. Integrins Play a Critical Role in Mechanical Stress-Induced p38 MAPK Activation. Hypertension 2002;39:233-238.

43. Nadruz W, Jr., Corat MAF, Marin TM, Guimaraes Pereira GA, Franchini KG. Focal adhesion kinase mediates MEF2 and c-Jun activation by stretch: Role in the activation of the cardiac hypertrophic genetic program. Cardiovasc Res 2005;68:87-97.

44. Lu H, Fedak PWM, Dai X, Du C, Zhou Y, Henkelman M, Mongroo PS, Lau A, Yamabi H, Hinek A, Husain M, Hannigan G, Coles JG. Integrin-Linked Kinase

Expression Is Elevated in Human Cardiac Hypertrophy and Induces Hypertrophy in Transgenic Mice. Circulation 2006;114:2271-2279.

45. Wu C, Dedhar S. Integrin-linked kinase (ILK) and its interactors: a new paradigm for the coupling of extracellular matrix to actin cytoskeleton and signaling complexes. J Cell Biol 2001;155:505-510.

46. Kim C, Cho Y, Chun Y, Park J, Kim M. Early Expression of Myocardial HIF-1{alpha} in Response to Mechanical Stresses: Regulation by Stretch-Activated Channels and the Phosphatidylinositol 3-Kinase Signaling Pathway. Circ Res 2002;90:e25-33.

47. White DE, Coutu P, Shi Y, Tardif J, Nattel S, St. Arnaud R, Dedhar S, Muller WJ. Targeted ablation of ILK from the murine heart results in dilated cardiomyopathy and spontaneous heart failure. Genes Dev 2006;20:2355-2360.

48. Legate KR, Montañez E, Kudlacek O, Fässler R. ILK, PINCH and parvin: the tIPP of integrin signalling. Nat Rev Mol Cell Biol 2006;7:20-31.

49. Pham CG, Harpf AE, Keller RS, Vu HT, Shai S, Loftus JC, Ross RS. Striated muscle-specific beta 1D-integrin and FAK are involved in cardiac myocyte hypertrophic response pathway. Am J Physiol Heart Circ Physiol 2000;279:H2916-2926.

50. Fassler R, Meyer M. Consequences of lack of beta 1 integrin gene expression in mice. Genes Dev 1995;9:1896-1908.

51. Shai S, Harpf AE, Babbitt CJ, Jordan MC, Fishbein MC, Chen J, Omura M, Leil TA, Becker KD, Jiang M, Smith DJ, Cherry SR, Loftus JC, Ross RS. Cardiac Myocyte-Specific Excision of the {beta}1 Integrin Gene Results in Myocardial Fibrosis and Cardiac Failure. Circ Res 2002;90:458-464.

52. Babbitt CJ, Shai S, Harpf AE, Pham CG, Ross RS. Modulation of integrins and integrin signaling molecules in the pressure-loaded murine ventricle. Histochem Cell Biol 2002;118:431-439.

53. Keller RS, Shai S, Babbitt CJ, Pham CG, Solaro RJ, Valencik ML, Loftus JC, Ross RS. Disruption of Integrin Function in the Murine Myocardium Leads to Perinatal Lethality, Fibrosis, and Abnormal Cardiac Performance. Am J Pathol 2001;158:1079-1090.

54. Ziegler WH, Liddington RC, Critchley DR. The structure and regulation of vinculin. Trends Cell Biol 2006;16:453-460.

55. Calderwood DA, Zent R, Grant R, Rees DJG, Hynes RO, Ginsberg MH. The Talin Head Domain Binds to Integrin beta Subunit Cytoplasmic Tails and Regulates Integrin Activation. J Biol Chem 1999;274:28071-28074.

56. Chen H, Cohen DM, Choudhury DM, Kioka N, Craig SW. Spatial distribution and functional significance of activated vinculin in living cells. J Cell Biol 2005;169:459-470.

57. Gallant ND, Michael KE, Garcia AJ. Cell Adhesion Strengthening: Contributions of Adhesive Area, Integrin Binding, and Focal Adhesion Assembly. Mol Biol Cell 2005;16:4329-4340.

58. Alenghat FJ, Fabry B, Tsai KY, Goldmann WH, Ingber DE. Analysis of Cell Mechanics in Single Vinculin-Deficient Cells Using a Magnetic Tweezer. Biochemical and Biophysical Research Communications 2000/10/14;277:93-99.

59. Subauste MC, Pertz O, Adamson ED, Turner CE, Junger S, Hahn KM. Vinculin modulation of paxillin-FAK interactions regulates ERK to control survival and motility. J Cell Biol 2004;165:371-381.

60. Xu W, Baribault H, Adamson E. Vinculin knockout results in heart and brain defects during embryonic development. Development 1998;125:327-337.

61. Zemljic-Harpf AE, Ponrartana S, Avalos RT, Jordan MC, Roos KP, Dalton ND, Phan VQ, Adamson ED, Ross RS. Heterozygous Inactivation of the Vinculin Gene Predisposes to Stress-Induced Cardiomyopathy. Am J Pathol 2004;165:1033-1044.

62. Zemljic-Harpf AE, Miller JC, Henderson SA, Wright AT, Manso AM, Elsherif L, Dalton ND, Thor AK, Perkins GA, McCulloch AD, Ross RS. Cardiac-Myocyte-Specific Excision of the Vinculin Gene Disrupts Cellular Junctions, Causing Sudden Death or Dilated Cardiomyopathy. Mol Cell Biol 2007;27:7522-7537.

63. Carmeliet P, Collen D. Transgenic mouse models in angiogenesis and cardiovascular disease. J Pathol 2000;190:387-405.

64. Takaoka H, Esposito G, Mao L, Suga H, Rockman HA. Heart size-independent analysis of myocardial function in murine pressure overload hypertrophy. Am J Physiol Heart Circ Physiol 2002;282:2190-2197.

65. Yang Z, Berr SS, Gilson WD, Toufektsian MC, French BA. Simultaneous evaluation of infarct size and cardiac function in intact mice by contrast-enhanced cardiac magnetic resonance imaging reveals contractile dysfunction in noninfarcted regions early after myocardial infarction. Circulation 2004;109:1161-1167.

66. Chien KR. Genes and physiology: molecular physiology in genetically engineered animals. J Clin Invest 1996;97:901-909.

67. Tanaka N, Dalton N, Mao L, Rockman HA, Peterson KL, Gottshall KR, Hunter JJ, Chien KR, Ross J,Jr. Transthoracic echocardiography in models of cardiac disease in the mouse. Circulation 1996;94:1109-1117.

68. Nahrendorf M, Badea C, Hedlund LW, Figueiredo JL, Sosnovik DE, Johnson GA, Weissleder R. High-resolution imaging of murine myocardial infarction with delayed-enhancement cine micro-CT. Am J Physiol Heart Circ Physiol 2007;292:H3172-8.

69. Franco F, Dubois SK, Peshock RM, Shohet RV. Magnetic resonance imaging accurately estimates LV mass in a transgenic mouse model of cardiac hypertrophy. Am J Physiol 1998;274:H679-83.

70. Croisille P, Rotaru C, Janier M, Hiba B. Gender and Strain Variations in Left Ventricular Cardiac Function and Mass Determined With Magnetic Resonance Imaging at 7 Tesla in Adult Mice. Invest Radiol 2007;42:1-7.

71. Wiesmann F, Frydrychowicz A, Rautenberg J, Illinger R, Rommel E, Haase A, Neubauer S. Analysis of right ventricular function in healthy mice and a murine model of heart failure by in vivo MRI. Am J Physiol Heart Circ Physiol 2002;283:H1065-71.

72. Alcalai R, Metzger S, Rosenheck S, Meiner V, Chajek-Shaul T. A recessive mutation in desmoplakin causes arrhythmogenic right ventricular dysplasia, skin disorder, and woolly hair. J Am Coll Cardiol 2003;42:319-327.

73. Suarez J, Gloss B, Belke DD, Hu Y, Scott B, Dieterle T, Kim YK, Valencik ML, McDonald JA, Dillmann WH. Doxycycline inducible expression of SERCA2a improves calcium handling and reverts cardiac dysfunction in pressure overload-induced cardiac hypertrophy. Am J Physiol Heart Circ Physiol 2004;287:H2164-72.

74. Jamora C, Fuchs E. Intercellular adhesion, signalling and the cytoskeleton. Nat Cell Biol 2002;4:E101-E108.

75. Kerckhoffs RCP, Narayan SM, Omens JH, Mulligan LJ, McCulloch AD. Computational Modeling for Bedside Application. Heart Failure Clinics 2008;4:371-378.

76. Christensen G, Wang Y, Chien KR. Physiological assessment of complex cardiac phenotypes in genetically engineered mice. Am J Physiol 1997;272:H2513-24.

77. Hasenfuss G. Animal models of human cardiovascular disease, heart failure and hypertrophy. Cardiovasc Res 1998;39:60-76.

78. Costandi PN, Frank LR, McCulloch AD, Omens JH. Role of diastolic properties in the transition to failure in a mouse model of the cardiac dilatation. Am J Physiol Heart Circ Physiol 2006;291:2971-2979.

79. Kubota T, McTiernan CF, Frye CS, Slawson SE, Lemster BH, Koretsky AP, Demetris AJ, Feldman AM. Dilated cardiomyopathy in transgenic mice with cardiac-specific overexpression of tumor necrosis factor-alpha. Circ Res 1997;81:627-635.

80. Ross AJ, Yang Z, Berr SS, Gilson WD, Petersen WC, Oshinski JN, French BA. Serial MRI evaluation of cardiac structure and function in mice after reperfused myocardial infarction. Magnetic Resonance in Medicine 2002;47:1158-1168.

81. Henson RE, Song SK, Pastorek JS, Ackerman JJH, Lorenz CH. Left ventricular torsion is equal in mice and humans. Am J Physiol Heart Circ Physiol 2000;278:H1117-H1123.

82. Liu W, Ashford MW, Chen J, Watkins MP, Williams TA, Wickline SA, Yu X. MR tagging demonstrates quantitative differences in regional ventricular wall motion in mice, rats, and men. Am J Physiol Heart Circ Physiol 2006;291:H2515-2521.

83. Epstein FH, Yang Z, Gilson WD, Berr SS, Kramer CM, French BA. MR tagging early after myocardial infarction in mice demonstrates contractile dysfunction in adjacent and remote regions. Magnetic Resonance in Medicine 2002;48:399-403.

84. Heijman E, Strijkers GJ, Habets J, Janssen B, Nicolay K. Magnetic resonance imaging of regional cardiac function in the mouse. MAGMA 2004;17:170-178.

85. Zhong J, Liu W, Yu X. Transmural myocardial strain in mouse: quantification of high-resolution MR tagging using harmonic phase (HARP) analysis. Magn Reson Med 2009;61:1368-1373.

86. Li G, Feng J, Yue L, Carrier M. Transmural heterogeneity of action potentials and Ito1 in myocytes isolated from the human right ventricle. Am J Physiol Heart Circ Physiol 1998;275:H369-377.

87. Davis JS, Hassanzadeh S, Winitsky S, Lin H, Satorius C, Vemuri R, Aletras AH, Wen H, Epstein ND. The overall pattern of cardiac contraction depends on a spatial gradient of myosin regulatory light chain phosphorylation. Cell 2001;107:631-641.

88. Shai S, Harpf A, Babbitt C, Jordan M, Fishbein M, Chen J, Omura M, Leil T, Becker KD, Jiang M, Smith D, Cherry S, Loftus J, Ross R. Cardiac Myocyte-Specific Excision of the {beta}1 Integrin Gene Results in Myocardial Fibrosis and Cardiac Failure. Circ Res 2002;90:458-464.

89. Moore CC, McVeigh ER, Zerhouni EA. Noninvasive measurement of three-dimensional myocardial deformation with tagged magnetic resonance imaging during graded local ischemia. J Cardiovasc Magn Reson 1999;1:207-222.

90. Moore CC, O'Dell WG, McVeigh ER, Zerhouni EA. Calculation of three-dimensional left ventricular strains from biplanar tagged MR images. J Magn Reson Imaging 1992;2:165-175.

91. Moore CC, Lugo-Olivieri CH, McVeigh ER, Zerhouni EA. Three-dimensional systolic strain patterns in the normal human left ventricle: characterization with tagged MR imaging. Radiology 2000;214:453-466.

92. Kuijer JP, Marcus JT, Gotte MJ, van Rossum AC, Heethaar RM. Three-dimensional myocardial strains at end-systole and during diastole in the left ventricle of normal humans. J Cardiovasc Magn Reson 2002;4:341-351.

93. O'Dell WG, Moore CC, Hunter WC, Zerhouni EA, McVeigh ER. Three-dimensional myocardial deformations: calculation with displacement field fitting to tagged MR images. Radiology 1995;195:829-835.

94. Jia Zhong, Wei Liu,Xin Yu,. Characterization of three-dimensional myocardial deformation in the mouse heart: An MR tagging study. Journal of Magnetic Resonance Imaging 2008;27:1263-1270.

95. Young AA, French BA, Yang Z, Cowan BR, Gilson WD, Berr SS, Kramer CM, Epstein FH. Reperfused myocardial infarction in mice: 3D mapping of late gadolinium enhancement and strain. J Cardiovasc Magn Reson 2006;8:685-692.

96. Axel L, Dougherty L. MR imaging of motion with spatial modulation of magnetization. Radiology 1989;171:841-845.

97. Yushkevich PA, Piven J, Hazlett HC, Smith RG, Ho S, Gee JC, Gerig G. User-guided 3D active contour segmentation of anatomical structures: Significantly improved efficiency and reliability. Neuroimage 2006;31:1116-1128.

98. Osman NF, Kerwin WS, McVeigh ER, Prince JL. Cardiac motion tracking using CINE harmonic phase (HARP) magnetic resonance imaging. Magnetic Resonance in Medicine 1999;42:1048-1060.

99. Vetter FJ, McCulloch AD. Three-dimensional analysis of regional cardiac function: a model of rabbit ventricular anatomy. Prog Biophys Mol Biol 1998;69:157-183.

100. Young AA, Orr R, Smaill BH, Dell'Italia LJ. Three-dimensional changes in left and right ventricular geometry in chronic mitral regurgitation. Am J Physiol Heart Circ Physiol 1996;271:H2689-2700.

101. Mazhari R, Omens JH, Waldman LK, McCulloch AD. Regional myocardial perfusion and mechanics: a model-based method of analysis. Ann Biomed Eng 1998;26:743-755.

102. Kuijer JPA, Jansen E, Marcus JT, Rossum ACv, Heethaar RM. Improved harmonic phase myocardial strain maps. Magnetic Resonance in Medicine 2001;46:993-999.

103. Chen T, Wang X, Chung S, Metaxas D, Axel L. Automated 3D motion tracking using Gabor filter bank, robust point matching, and deformable models. IEEE Trans Med Imaging 2010;29:1-11.

104. Young AA, Kraitchman DL, Dougherty L, Axel L. Tracking and finite element analysis of stripe deformation in magnetic resonance tagging. Medical Imaging, IEEE Transactions on 1995;14:413-421.

105. Chuang J, McCulloch A, Omens J, Frank L. Generation of an accurate 3D computational model of the mouse heart from MR images. 2007.

106. Costandi PN, McCulloch AD, Omens JH, Frank LR. High-resolution longitudinal MRI of the transition to heart failure. Magn Reson Med 2007;57:714-720.

107. Stegger L, Heijman E, Schafers KP, Nicolay K, Schafers MA, Strijkers GJ. Quantification of left ventricular volumes and ejection fraction in mice using PET, compared with MRI. J Nucl Med 2009;50:132-138.

108. McCulloch AD, Omens JH. Non-homogeneous analysis of three-dimensional transmural finite deformation in canine ventricular myocardium. J Biomech 1991;24:539-548.

109. Ashikaga H, Omens JH, Ingels NB,Jr, Covell JW. Transmural mechanics at left ventricular epicardial pacing site. Am J Physiol Heart Circ Physiol 2004;286:H2401-7.

110. Young AA, Dokos S, Powell KA, Sturm B, McCulloch AD, Starling RC, McCarthy PM, White RD. Regional heterogeneity of function in nonischemic dilated cardiomyopathy. Cardiovasc Res 2001;49:308-318.

111. Tanaka N, Tone T, Ono S, Tomochika Y, Murata K, Kawagishi T, Yamazaki N, Matsuzaki M. Predominant Inner-Half Wall Thickening of Left Ventricle Is Attenuated

in Dilated Cardiomyopathy: An Application of Tissue Doppler Tracking Technique. Journal of the American Society of Echocardiography 2001;14:97-103.

112. Kanzaki H, Nakatani S, Yamada N, Urayama S, Miyatake K, Kitakaze M. Impaired systolic torsion in dilated cardiomyopathy: reversal of apical rotation at mid-systole characterized with magnetic resonance tagging method. Basic Res Cardiol 2006;101:465-470.

113. Dumesnil JG, Shoucri RM. Quantitative relationships between left ventricular ejection and wall thickening and geometry. J Appl Physiol 1991;70:48-54.

114. Omens JH, Usyk TP, Li Z, McCulloch AD. Muscle LIM protein deficiency leads to alterations in passive ventricular mechanics. Am J Physiol Heart Circ Physiol 2002;282:H680-H687.

115. Jiang Y, Pandya K, Smithies O, Hsu EW. Three-dimensional diffusion tensor microscopy of fixed mouse hearts. Magn Reson Med 2004;52:453-460.

116. Ho SY, Jackson M, Kilpatrick L, Smith A, Gerlis LM. Fibrous matrix of ventricular myocardium in tricuspid atresia compared with normal heart. A quantitative analysis. Circulation 1996;94:1642-1646.

117. Clark KA, McElhinny AS, Beckerle MC, Gregorio CC. STRIATED MUSCLE CYTOARCHITECTURE: An Intricate Web of Form and Function. Annu Rev Cell Dev Biol 2002;18:637-706.

118. Granzier HL, Labeit S. The giant protein titin: a major player in myocardial mechanics, signaling, and disease. Circ Res 2004;94:284-295.

119. Robinson TF, Geraci MA, Sonnenblick EH, Factor SM. Coiled perimysial fibers of papillary muscle in rat heart: morphology, distribution, and changes in configuration. Circ Res 1988;63:577-592.

120. Grossman W, Barry WH. Diastolic pressure-volume relations in the diseased heart. Fed Proc 1980;39:148-155.

121. Lorenzen-Schmidt I, Stuyvers BD, ter Keurs HEDJ, Date M, Hoshijima M, Chien KR, McCulloch AD, Omens JH. Young MLP deficient mice show diastolic dysfunction before the onset of dilated cardiomyopathy. J Mol Cell Cardiol 2005;39:241-250.

122. Goldmann WH, Galneder R, Ludwig M, Xu W, Adamson ED, Wang N, Ezzell RM. Differences in Elasticity of Vinculin-Deficient F9 Cells Measured by Magnetometry and Atomic Force Microscopy. Exp Cell Res 1998;239:235-242.

123. Sohal DS, Nghiem M, Crackower MA, Witt SA, Kimball TR, Tymitz KM, Penninger JM, Molkentin JD. Temporally Regulated and Tissue-Specific Gene Manipulations in the Adult and Embryonic Heart Using a Tamoxifen-Inducible Cre Protein. Circ Res 2001.

124. Raskin AM, Hoshijima M, Swanson E, McCulloch AD, Omens JH. Hypertrophic gene expression induced by chronic stretch of excised mouse heart muscle. Mol Cell Biomech 2009;6:145-159.

125. Raskin A. Four and Half LIM Domain-1 Protein and its Role in Passive Mechanics and Hypertrophic Signaling of the Heart. 2008.

126. Wu Y, Cazorla O, Labeit D, Labeit S, Granzier H. Changes in titin and collagen underlie diastolic stiffness diversity of cardiac muscle. J Mol Cell Cardiol 2000;32:2151-2162.

127. MacKenna DA, Vaplon SM, McCulloch AD. Microstructural model of perimysial collagen fibers for resting myocardial mechanics during ventricular filling. Am J Physiol 1997;273:H1576-86.

128. Villarreal F, Omens J, Dillmann W, Risteli J, Nguyen J, Covell J. Early degradation and serum appearance of type I collagen fragments after myocardial infarction. J Mol Cell Cardiol 2004;36:597-601.

129. Weis SM, Emery JL, Becker KD, McBride DJ,Jr, Omens JH, McCulloch AD. Myocardial mechanics and collagen structure in the osteogenesis imperfecta murine (oim). Circ Res 2000;87:663-669.

130. Johnatty SE, Dyck JRB, Michael LH, Olson EN, Abdellatif M. Identification of Genes Regulated During Mechanical Load-induced Cardiac Hypertrophy. Journal of Molecular and Cellular Cardiology, 2000;32:805-815.

131. McGrath MF, de Bold AJ. Determinants of natriuretic peptide gene expression. Peptides, 2005;26:933-943.

132. Ruwhof C, vanderLaarse A. Mechanical stress-induced cardiac hypertrophy: mechanisms and signal transduction pathways. Cardiovascular Research 2000;47:23-37.

133. Komuro I, Kudo S, Yamazaki T, Zou Y, Shiojima I, Yazaki Y. Mechanical stretch activates the stress-activated protein kinases in cardiac myocytes. FASEB J 1996;10:631-636.

134. Sadoshima J, Jahn L, Takahashi T, Kulik TJ, Izumo S. Molecular characterization of the stretch-induced adaptation of cultured cardiac cells. An in vitro model of load-induced cardiac hypertrophy. J Biol Chem 1992;267:10551-10560.

135. van Wamel AJ, Ruwhof C, van der Valk-Kokshoorn LJ, Schrier PI, van der Laarse A. Rapid effects of stretched myocardial and vascular cells on gene expression of neonatal rat cardiomyocytes with emphasis on autocrine and paracrine mechanisms. Arch Biochem Biophys 2000;381:67-73.

136. Yamazaki T, Komuro I, Kudoh S, Zou Y, Shiojima I, Mizuno T, Takano H, Hiroi Y, Ueki K, Tobe K. Mechanical stress activates protein kinase cascade of phosphorylation in neonatal rat cardiac myocytes. J Clin Invest 1995;96:438-446.

137. Sindhu M. Gopalan, Chris Flaim, Sangeeta N. Bhatia, Masahiko Hoshijima, Ralph Knoell, Kenneth R. Chien, Jeffrey H. Omens,Andrew D.McCulloch,. Anisotropic stretch-induced hypertrophy in neonatal ventricular myocytes micropatterned on deformable elastomers. Biotechnol Bioeng 2003;81:578-587.

138. Simpson DG, Majeski M, Borg TK, Terracio L. Regulation of Cardiac Myocyte Protein Turnover and Myofibrillar Structure In Vitro by Specific Directions of Stretch. Circ Res 1999;85:e59-69.

139. Simpson DG, Majeski M, Borg TK, Terracio L. Regulation of Cardiac Myocyte Protein Turnover and Myofibrillar Structure In Vitro by Specific Directions of Stretch. Circ Res 1999;85:e59-69.

140. Senyo SE, Koshman YE, Russell B. Stimulus interval, rate and direction differentially regulate phosphorylation for mechanotransduction in neonatal cardiac myocytes. FEBS Lett 2007;581:4241-4247.

141. Knoll R, Hoshijima M, Hoffman HM, Person V, Lorenzen-Schmidt I, Bang ML, Hayashi T, Shiga N, Yasukawa H, Schaper W, McKenna W, Yokoyama M, Schork NJ, Omens JH, McCulloch AD, Kimura A, Gregorio CC, Poller W, Schaper J, Schultheiss HP, Chien KR. The cardiac mechanical stretch sensor machinery involves a Z disc complex that is defective in a subset of human dilated cardiomyopathy. Cell 2002;111:943-955.

142. Hoshijima M. Mechanical stress-strain sensors embedded in cardiac cytoskeleton: Z disk, titin, and associated structures. Am J Physiol Heart Circ Physiol 2006;290:H1313-1325.

143. Jaalouk DE, Lammerding J. Mechanotransduction gone awry. Nat Rev Mol Cell Biol 2009;10:63-73.

144. Duffy DC, McDonald JC, Schueller OJA, Whitesides GM. Rapid Prototyping of Microfluidic Systems in Poly(dimethylsiloxane). Anal Chem 1998;70:4974-4984.

145. Pham CG, Harpf AE, Keller RS, Vu HT, Shai S, Loftus JC, Ross RS. Striated muscle-specific beta 1D-integrin and FAK are involved in cardiac myocyte hypertrophic response pathway. Am J Physiol Heart Circ Physiol 2000;279:H2916-2926.

146. Camelliti P, Gallagher JO, Kohl P, McCulloch AD. Micropatterned cell cultures on elastic membranes as an in vitro model of myocardium. Nat Protocols 2006;1:1379-1391.

147. Sindhu M. Gopalan, Chris Flaim, Sangeeta N. Bhatia, Masahiko Hoshijima, Ralph Knoell, Kenneth R. Chien, Jeffrey H. Omens,Andrew D.McCulloch,. Anisotropic stretch-induced hypertrophy in neonatal ventricular myocytes micropatterned on deformable elastomers. Biotechnol Bioeng 2003;81:578-587.

148. Motlagh D, Hartman TJ, Desai TA, Russell B. Microfabricated grooves recapitulate neonatal myocyte connexin43 and N-cadherin expression and localization. Journal of Biomedical Materials Research Part A 2003;67A:148-157.

149. Cohn RD, Mayer U, Saher G, Herrmann R, van der Flier A, Sonnenberg A, Sorokin L, Voit T. Secondary reduction of α7B integrin in laminin α2 deficient congenital muscular dystrophy supports an additional transmembrane link in skeletal muscle. J Neurol Sci 1999;163:140-152.

150. Berrier AL, Mastrangelo AM, Downward J, Ginsberg M, LaFlamme SE. Activated R-ras, Rac1, PI 3-kinase and PKCepsilon can each restore cell spreading inhibited by isolated integrin beta1 cytoplasmic domains. J Cell Biol 2000;151:1549-1560.

151. Lukashev ME, Sheppard D, Pytela R. Disruption of integrin function and induction of tyrosine phosphorylation by the autonomously expressed beta 1 integrin cytoplasmic domain. J Biol Chem 1994;269:18311-18314.

152. Ross RS, Pham C, Shai SY, Goldhaber JI, Fenczik C, Glembotski CC, Ginsberg MH, Loftus JC. Beta1 integrins participate in the hypertrophic response of rat ventricular myocytes. Circ Res 1998;82:1160-1172.

153. Lal H, Verma SK, Smith M, Guleria RS, Lu G, Foster DM, Dostal DE. Stretch-induced MAP kinase activation in cardiac myocytes: differential regulation through beta1-integrin and focal adhesion kinase. J Mol Cell Cardiol 2007;43:137-147.

154. Chen YP, O'Toole TE, Shipley T, Forsyth J, LaFlamme SE, Yamada KM, Shattil SJ, Ginsberg MH. "Inside-out" signal transduction inhibited by isolated integrin cytoplasmic domains. J Biol Chem 1994;269:18307-18310.

155. MacKenna DA, Dolfi F, Vuori K, Ruoslahti E. Extracellular signal-regulated kinase and c-Jun NH2-terminal kinase activation by mechanical stretch is integrin-dependent and matrix-specific in rat cardiac fibroblasts. J Clin Invest 1998;101:301-310.

156. Samarel AM. Costameres, focal adhesions, and cardiomyocyte mechanotransduction. Am J Physiol Heart Circ Physiol 2005;289:H2291-2301.

157. Emery JL, Omens JH. Mechanical regulation of myocardial growth during volume-overload hypertrophy in the rat. Am J Physiol Heart Circ Physiol 1997;273:H1198-H1204.

158. Pfaff M, Liu S, Erle DJ, Ginsberg MH. Integrin beta cytoplasmic domains differentially bind to cytoskeletal proteins. J Biol Chem 1998;273:6104-6109.